

# Metamorphic modeling and petrochronology of metapelitic rocks from the Luminárias Nappe, southern Brasília belt (SE Brazil)

Regiane Andrade Fumes<sup>1\*</sup> , George Luiz Luvizotto<sup>1</sup> , Renato Moraes<sup>2</sup> ,  
Monica Heilbron<sup>3</sup> , Silvio Roberto Farias Vlach<sup>2</sup> 

## Abstract

The Luminárias Nappe was formed in the agglutination of West Gondwana. A high-pressure metamorphic gradient oblique to the geological contacts is recorded in metapelitic rocks from this Nappe. In the northern portion, the metamorphic peak conditions are at high-pressure lower-amphibolite facies at  $580 \pm 4^\circ\text{C}$  and ca. 0.9 GPa (Chl + Ky + St + Ms + Qtz + Rt); in the central portion, they are at high-pressure amphibolite facies at  $600 \pm 15^\circ\text{C}$  and  $1.1 \pm 0.3$  GPa (St + Bt + Grt + Ms + Qtz + Rt); and in the southern portion, they reach the eclogite facies at  $630 \pm 13^\circ\text{C}$  and  $1.4 \pm 0.6$  GPa (St + Ky + Grt + Ms + Qtz + Rt). Clockwise metamorphic P-T-t paths are registered in the studied rocks, with temperature and pressure increase followed by a strong decompression with retrograde phases as chloritoid (northern portion), chlorite and ilmenite (central portion) and biotite, chlorite and ilmenite (southern portion). U-Th-Pb<sub>T</sub> monazite ages range from  $632 \pm 4$  Ma (southern portion) to  $600 \pm 8$  Ma (northern portion included crystals in garnet and staurolite). The metamorphic age, the high-pressure conditions calculated in this paper and the clockwise metamorphic path indicate that the tectonic evolution of the Luminárias Nappe rocks is tightly associated with the subduction and collision processes of the southern Brasília belt. The overprint of the younger Ribeira belt is interpreted to be responsible for rock pile tilting, thus producing the oblique metamorphic gradient.

**KEYWORDS:** West Gondwana; monazite dating; THERMOCALC; single element geothermometer; pseudosection.

## INTRODUCTION

Pressure-temperature-time (P-T-t) paths of high-pressure rocks are key to understand the evolution of an orogen. High-pressure rocks are the main record of deep portions of continental crust formed in convergent plate boundaries. Furthermore, they provide an insight into geodynamic processes that transform the rocks from the crust and lithospheric mantle into metamorphic and igneous rocks (Möller *et al.* 2018). The root of Precambrian eroded orogens, such as the Brasília belt, Brazil, is crucial places to study high-pressure rocks. In eroded orogens, a variety of high-pressure metamorphic rocks is exposed for hundreds of kilometers, giving the opportunity to study processes that take place in convergent plate boundaries.

Thus, linking portions of the P-T path to ages, textures and equilibrium mineral assemblages are a main issue, since a well-defined P-T-t path may provide reliable information of metamorphic and tectonic processes. The concept of petrochronology has been introduced recently (Fraser *et al.* 1997) and deals with the fact that rocks face a complex history of heating, cooling, and exhumation and, therefore, do not record just a single age (Engi *et al.* 2017). This concept is especially useful in areas where orogenic processes are overprinted.

The Luminárias Nappe comprises a set of quartzite and metapelitic rocks that represent part of the passive margin sequence of the São Francisco Craton (*e.g.*, Paciullo *et al.*, 2000). This passive margin was metamorphosed during the Ediacaran-Cambrian orogenesis, which led to the agglutination of West Gondwana (Dardenne 2000, Fuck *et al.* 2017, Heilbron *et al.* 2017). There are controversial interpretations regarding the tectonic evolution of the Luminárias Nappe, that is, either in a single tectonic episode related to the formation of the southern Brasília belt (Campos Neto 2000, Campos Neto *et al.* 2004, 2007, 2011, Westin *et al.* 2016) or as part of the interference zone between the southern Brasília and Central Ribeira belts (Peternel *et al.* 2005, Trouw *et al.* 2000, 2013b, Heilbron *et al.* 2008, Coelho *et al.* 2017).

Previous regional studies in southern Brasília and central Ribeira belts describe a regional metamorphic gradient with conditions increasing from north to south and from east to west, from greenschist to granulite facies conditions (Trouw *et al.* 1980, Ribeiro & Heilbron 1982, Peternel *et al.* 2005, Reno *et al.* 2012, Trouw *et al.* 2000, 2013b (with a regional

### Supplementary data

Supplementary data associated with this article can be found in the online version: [Supplementary Table A1](#).

<sup>1</sup>Department of Petrology and Metallogeny, Universidade Estadual de São Paulo – Rio Claro (SP), Brazil. E-mails: regiane.fumes@unesp.br, georgell@rc.unesp.br

<sup>2</sup>Department of Mineralogy and Geotectonics, Universidade de São Paulo – São Paulo (SP), Brazil. E-mails: rmoraes@usp.br, srfvlach@usp.br

<sup>3</sup>TEKTOS Research Group, Geology Institute, Universidade do Estado do Rio de Janeiro – Rio de Janeiro (RJ), Brazil. E-mail: monica.heilbron@gmail.com

\*Corresponding author.



metamorphic map). Although numerous studies described the regional metamorphic gradient, they are mostly based on petrography and mineral assemblage of the rocks. Here, we present a more accurate and up-to-date approach in order to characterize the metamorphic conditions using pseudosection modeling, Zr-in-rutile and Ti-in-quartz thermometry, and *in situ* U-Th-Pb<sub>T</sub> monazite electron microprobe analysis (EPMA) dating. This paper aims to define metamorphic conditions, *P-T-t* paths and metamorphism age of metapelitic rocks from the Luminárias Nappe and, therefore, to contribute for understanding the tectonic framework of the southern Brasília and Ribeira belts.

## GEOLOGICAL SETTING

The Brasília belt borders the western margin of São Francisco Craton (Fig. 1) in central and southwestern Brazil. It extends for more than 1,100 km roughly in the N-S direction and is the record of the convergence and collision that took place during

the Brasiliano orogeny in the late Neoproterozoic, as part of West Gondwana amalgamation (Dardenne 2000, Fuck *et al.* 2017, Heilbron *et al.* 2017).

The Brasília belt is usually subdivided into northern and southern Brasília belts by the Pirineus Syntaxis (Araújo Filho 2000). The southern portion of the Brasília belt is dominated by metasedimentary rocks that underwent metamorphism and deformation during the Brasiliano orogeny, with metamorphic peak of *ca.* 650–630 Ma (Valeriano 2017). Most of these metasedimentary rocks represent stratigraphy sections from one of the former Neoproterozoic passive margins developed around the São Francisco paleocontinent (Valeriano 2017).

The metasedimentary rocks in the south of São Francisco Craton were originally grouped into the São João del Rei and Andrelândia Groups (Ebert 1956). Trouw *et al.* (1980) describe the metasedimentary rocks near Luminárias Nappe as the Carrancas Group, with intermediary characteristics between São João del Rei and Andrelândia Groups. The Carrancas Group is divided into São Tomé das Letras Formation, which

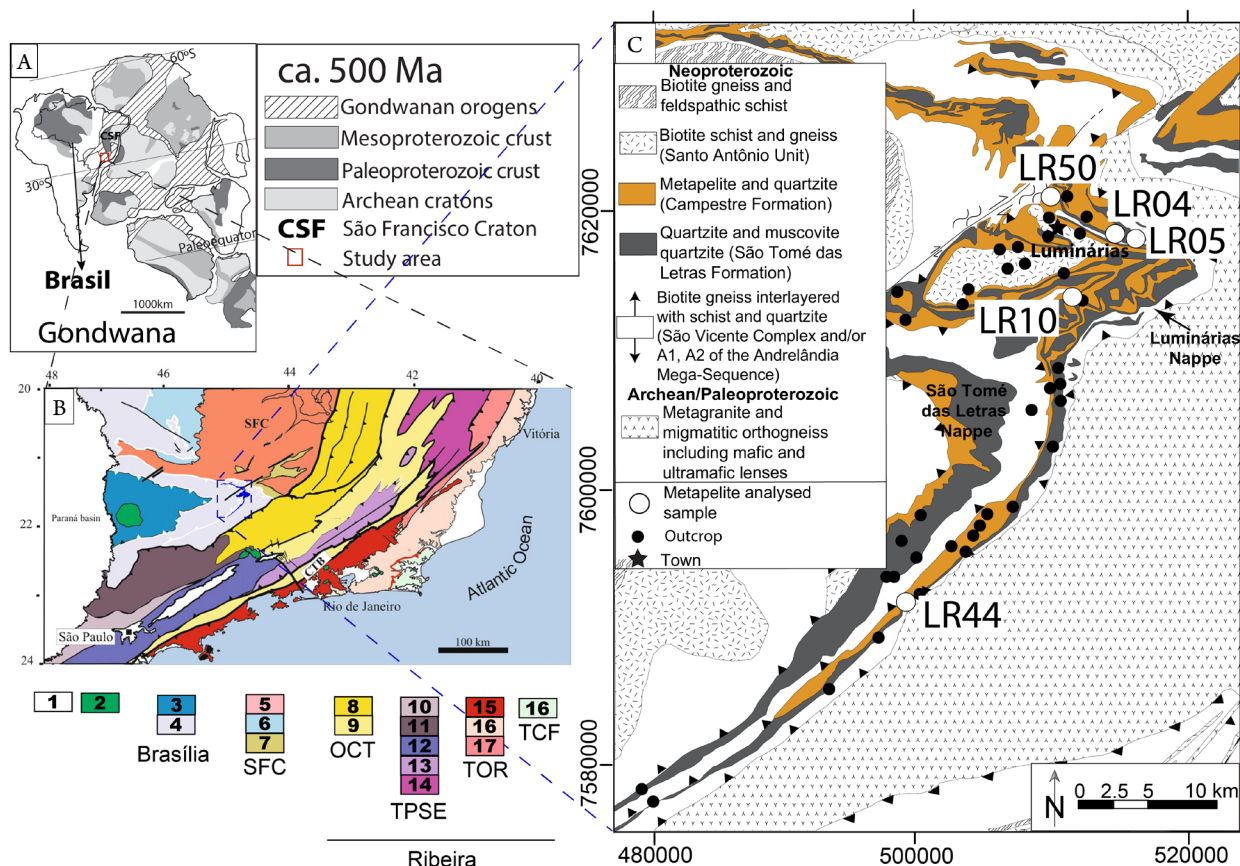


**Figure 1.** Geological setting of the study area. (A) Gondwana map (ca. 500 Ma) showing the location of the study area (red rectangle). Extracted from Spencer *et al.* (2013). (B) Tectonic framework of the Ribeira and Southern Brasília belts extract from Heilbron *et al.* (2017). 1. Phanerozoic cover; 2. Upper Cretaceous alkaline plutons; 3 and 4 east verging units of the Brasília Belt, including the Guaxupé nappe and lower nappes; 5-7 Units of the São Francisco craton: 5. Paleoproterozoic Archean basement, 6. Neoproterozoic cratonic cover, Bambuí Group, 7. Mesoproterozoic to Neoproterozoic metasediments of autochthonous domains; 7-16 Terranes and structural domains of the Ribeira Belt: 8. Andrelândia and 9. Juiz de Fora domains of Occidental terrane, 10. Socorro Nappe; 11. Apiaí terrane; 12. Embú terrane; 13. Paraíba do Sul terrane; 14. Cambuci terrane; 15. Cryogenean to Ediacaran magmatic arc, 16. Neoproterozoic metasedimentary successions and 13. Tonian magmatic arc of the Oriental terrane; 12. Cabo Frio terrane. (C) Simplified geological map of the Luminárias Nappe. Modified after Trouw *et al.* (2013a); Quéméneur *et al.* (2002); Nunes *et al.* (2008); Paciullo and Ribeiro (2008). The geological map of Luminárias sheet is based on Almeida (1992) and mapping of undergraduate courses in the 80ths of Federal University of Rio de Janeiro. The circles (white and black) show the localization of the studied metapelite samples. The arrows in the legend of the biotite gneiss interlayered with schists and quartzite is due the different interpretations presented in the literature of the age of this unit, according Ribeiro *et al.* (1995) and Paciullo *et al.* (2000) this unit is Neoproterozoic (A1 and A2), however according Westin *et al.* (2016) this is a Paleoproterozoic unit (São Vicente Complex). Geographical coordinates of analyzed samples are present in Table 1.

is composed of quartzite, and in the Campestre Formation, which is comprised of metapelites and quartzites (Trouw *et al.* 1980, 1983; Fig. 1). Almeida (1992) performed a detailed description of the geology, mapping the Luminárias region at 1:50,000 scale. Further papers (Paciullo *et al.* 2000, 2003) interpret the Carrancas Group as two formations within the Andrelândia Mega-sequence, which is divided into six lithofacies (A1, A2, A3, A4, A5, and A6). The Campestre Formation from Luminárias Nappe corresponds (Fig. 1) to the A4 lithofacies (Paciullo *et al.* 2000, 2003). The Mega-sequence is interpreted as formed in a transition between a rift to passive margin succession, developed along the southern margin of the São Francisco paleocontinent during the Neoproterozoic (Ribeiro *et al.* 1995, Paciullo *et al.* 2000). An alternative interpretation for the provenance of the basal lithofacies (A1 and A2 — biotite gneiss interlayered with schist and quartzite; Fig. 1, from Andrelândia Megasequence) is that these rocks belong to the Paleoproterozoic and have affinity with fore arc basin and trench deposits (Westin *et al.* 2016, 2019). According to Westin *et al.* (2016, 2019), the A1 and A2 lithofacies are called São Vicente Complex and are not related neither to the Carrancas Group nor Andrelândia Mega-sequence.

The metasedimentary rocks from the southern Brasília belt are organized in a stack of syn-metamorphic thick-skinned nappes (Campos Neto *et al.* 2010). From the structurally highest levels, in the west, to the structurally lowest levels, in the east, the following sequence of nappes is recognized:

- the Socorro-Guaxupé Nappe, which represents the middle and lower crust and is interpreted as the root of an intra-continental magmatic arc;
- the Andrelândia Nappe System that is composed of the Três Pontas-Varginha Nappe and associated klippen, as well as the Liberdade and Andrelândia nappes (Campos Neto *et al.* 2010);
- the Carrancas Nappe System and the Lima Duarte Nappe (Campos Neto *et al.* 2004, 2007, 2010, Westin & Campos Neto 2013, Westin *et al.* 2016), also known as Lower Nappe System (Fig. 1).

The Carrancas Nappe system is the farthest east and the deepest in the pile, including deformed rocks of the former passive continental margin located at the margin of São Francisco paleocontinent (Campos Neto *et al.* 2010). This Nappe system is composed of rocks from Carrancas Group (Trouw *et al.* 1980, 1983), associated with basement slices and is divided from structural top to bottom in São Tomé das Letras Nappe, Luminárias Nappe, Carrancas-Itumirim Klippe, Serra da

Bandeira allochthon, and Madre de Deus allochthon (Campos Neto *et al.* 2004).

The Brasília belt is in contact with the Neoproterozoic Ribeira belt on its southeastern border (Hasui *et al.* 1975, Trouw *et al.* 2000, Heilbron *et al.* 2000, 2004, 2008, 2017). Contrasting interpretations of this region were presented in literature, as it is either described as an interference zone between the Brasília and Ribeira belts, due to superposition of structures and metamorphism related to collision in both belts (Peternel *et al.* 2005, Trouw *et al.* 2000, 2013b, Heilbron *et al.* 2008, 2017, Coelho *et al.* 2017), or it is considered as formed exclusively due to metamorphism and deformation associated with the Brasília Orogeny (Campos Neto 2000, Campos Neto *et al.* 2004, 2007, 2011, Westin *et al.* 2016).

Metamorphic conditions of Brasília belt rocks increase westwards from non-metamorphic and low-greenschist facies rocks, at the cratonic border in the east to high-temperature amphibolite to granulite facies rocks, up to ultra-high temperature conditions in the metamorphic core (Moraes *et al.* 2002, 2015), and decrease again westwards to amphibolite and greenschist facies towards the Goiás Magmatic Arc (Fuck *et al.* 2017). Previous metamorphic studies in the Carrancas Group rocks from the Luminárias Nappe show a metamorphic gradient, increasing from greenschist facies, in the north, to amphibolite facies, in the south (Trouw *et al.* 1980, Ribeiro & Heilbron 1982, Peternel *et al.* 2005, Reno *et al.* 2012, Trouw *et al.* 2000, 2013b). According to Campos Neto & Caby (1999), the metamorphic conditions of Carrancas Group rocks (correlated with the study rocks) are high pressure and low temperature, with metamorphic assemblage garnet-kyanite-chloritoid. Silva (2010) described in the Carrancas Klippe, also composed of rocks from Carrancas Group, a metamorphic gradient that increases to the southeast, from upper greenschist facies to high pressure amphibolite facies in the transition to eclogite facies. A recent study in the metapelitic rocks of the Luminárias Nappe using the average PT mode of THERMOCALC indicates the presence of a metamorphic gradient with conditions increasing from greenschist/amphibolite facies, in the northern and center-northern portion, to amphibolite/eclogite facies in the southern portion (Fumes *et al.* 2017).

Neoproterozoic ages of metamorphism, peak and retrograde, from whole southern Brasília belt vary, from 670 to 590 Ma (Vlach & Gualda 2000, Campos Neto *et al.* 2004, Valeriano *et al.* 2004, Campos Neto *et al.* 2007, Campos Neto *et al.* 2010, 2011, Trouw *et al.* 2008, Reno *et al.* 2010, 2012, Westin *et al.* 2016, Coelho *et al.* 2017, Rocha *et al.* 2017, 2018, Tedeschi *et al.* 2017, 2018). Monazite ages obtained with laser ablation-inductively coupled plasma-mass spectrometry (LA-ICP-MS) from the Carrancas Klippe rocks (northeast of the Luminárias Nappe) are ca. 590-575 Ma (Valeriano *et al.* 2004, Campos Neto *et al.* 2010). According to Campos Neto *et al.* (2010, 2011), the younger ages of ca. 590 Ma determined for the Carrancas rocks represent the propagation and migration of the deformation and metamorphism through the pile of nappes, from the upper to the lower nappes, in which Luminárias Nappe is included. Alternatively, the younger ages can be interpreted as an effect of the Ribeira belt overprint.

**Table 1.** Location of the analyzed samples. Coordinates are in UTM (Zone 23K, WGS84).

Analyzed sample	UTME	UTMS
LR04	516069	7620512
LR05	516522	7619845
LR10	513194	7615681
LR44	501284	7593736
LR50	510651	7604100

## LOCAL GEOLOGY

The Luminárias Nappe crops out in a ca. 80 km long N-S elongated nappe, near Luminárias town in Minas Gerais, southeastern Brazil. In the northern portion of the study area (Fig. 1C), rocks from the Luminárias Nappe present an irregular exposure pattern due to low-dipping folded layers exposed on a steep topography. Observed outcrops and collected samples cover the whole extent of the Luminárias Nappe (Fig. 1, Tab. 1 and Suppl. Tab. 1).

The Luminárias Nappe was thrust over the basement rocks, which are composed of metagranite and migmatitic orthogneiss, with lenses of mafic and ultramafic rocks. The basement is overthrust by biotite gneiss, interlayered with schist and quartzite from the São Vicente Complex and/or the basal formation of Andrelândia Mega-sequence (A1, A2). A group of quartzite and muscovite quartzite occurs on the top of the biotite gneiss (São Tomás das Letras Formation). At its top, the Campestre Formation crops out that is composed of metapelitic rocks, which are the focus of this paper, and quartzite. The uppermost unit of the Luminárias Nappe is composed of biotite schist and gneiss from Santo Antônio Unit.

Deformational structures in the Luminárias Nappe region are grouped into three successive deformational phases ( $D_1$ ,  $D_2$  and  $D_3$ ). The deformational phases  $D_1$  and  $D_2$  are related and responsible for the main flat lying composite foliation  $S_1/S_2$  (Campos Neto & Caby 1999, Campos Neto 2000, Trouw *et al.* 2000, Trouw *et al.* 2008). Locally, these two phases can be distinguished using interference structures, such as fold and foliation overprint. Therefore,  $D_1$  and  $D_2$  are interpreted as representing a single progressive deformation related to later stages of subduction and continental collision (Trouw *et al.* 2008). As proposed by Trouw *et al.* (2008), the main foliation observed in the rocks is a result of  $D_1$  and  $D_2$  deformational phases and is labeled here as  $S_{1/2}$ . The classification of foliations and kinematic interpretations of porphyroblasts presented here are according Passchier & Trouw (2005). The  $S_{1/2}$  foliation often occurs as a continuous foliation or as a slaty cleavage in the northern portion, and as schistosity in the southern portion of the Luminárias Nappe (Fig. 2A to I). Sometimes,  $S_{1/2}$  occurs as a crenulation cleavage, where it is possible to identify the older  $S_1$  foliation preserved in micro-lithons. Depending on the location of the rocks along the Luminárias Nappe, the main foliation  $S_{1/2}$  is marked by different minerals, reflecting the metamorphic gradient. The relation between the porphyroblasts and the main foliation changes as well. For instance, in the northern portion, the chloritoid porphyroblasts do not present strain shadows and deflection of external foliation around the porphyroblasts (Fig. 2B). This is a different situation from the garnet porphyroblasts in the southern portion, which present strain shadows and deflection of external foliation around them (Fig. 2G).

## MATERIALS AND METHODS

The analytical work was performed at the laboratories of the Department of Petrology and Metallogeny of São Paulo State University, Brazil, except for the LA-ICP-MS analysis, carried

out at the Micro-geochemistry Laboratory of the Department of Earth Sciences at the University of Gothenburg, Sweden.

Petrography was carried out in polished thin sections (see locations in Fig. 1 and Tab. 1) using optical and scanning electron microscopes (SEM). A JEOL JSM 6010LA SEM was used under a column, accelerating voltage of 15 kV and varied beam currents to obtain backscattered electron images (BSE).

## Whole-rock chemistry and pseudosection

Whole-rock chemical compositions for 11 samples were obtained through X-ray fluorescence. Representative sample powders were mixed with lithium tetraborate to obtain fused disks, which were analyzed with a Philips PW 2400 equipment. Loss on ignition (LOI) was determined by the conventional gravimetric method.

Two  $P$ - $T$  pseudosections were calculated for samples LR10C and LR44C, using the THERMOCALC (Powell & Holland 1988, Powell *et al.* 1998), version 3.40, and the internally consistent thermodynamic dataset tc-ds62 from Holland and Powell (2011), updated in February 2012. All calculations were based on the chemical model system  $K_2O$ - $FeO$ - $MgO$ - $Al_2O_3$ - $SiO_2$ - $H_2O$ - $TiO_2$ - $O_2$  (KFMASHTO), which represents a pelitic composition with the addition of  $TiO_2$  and  $O_2$  in order to evaluate rutile and ilmenite stability. As all samples lack plagioclase and present very low CaO (LR10C = 0.51 wt.%, LR44C = 0.15 wt.%) and  $Na_2O$  (LR10C = 0.35 wt.%, LR44C = 0.28 wt.%) content, these oxides were not considered in the investigated model system. Oxygen ( $O_2$ ) content was estimated as suggested by White *et al.* (2000) and, since the studied samples are ilmenite and rutile bearing free of hematite, a low O (0.11 mol.%) value was used.

## Electron microprobe analysis

The chemical mineral analysis was carried out through wavelength dispersive spectrometry (WDS) using a JEOL JXA-8230 Electron Microprobe equipped with five WDS detectors. Matrix correction was carried out online by the software provided through JEOL, using the ZAF (Z as atomic number, A as absorption and F as fluorescence) method.

Garnet, chlorite, chloritoid, staurolite, biotite, and muscovite were analyzed under a 15 kV and 20 nA focused beam for the column accelerating voltage and beam current, respectively. Point analyses were carried out in the core and rim of minerals, as well as core-rim profiles, considering total counting times of 20 and 30 seconds for major and minor elements, respectively, which are equally distributed on peak and background positions. Minerals and synthetic oxides, as referenced on the laboratory, were used as standards. Mineral formulae were computed with the AX software (Holland & Powell 2000).

Analyses of trace elements in rutile were made using a focused beam at 20 kV and 80 nA, following the method outlined by Luvizotto *et al.* (2009). Si, Al, Cr, Fe, Ta, Nb, and Zr were measured and Si concentrations were used as a quality control to detect and avoid zircon inclusions, as well as contaminations. Based on the recommendation of Zack *et al.* (2004), measurements with Si concentrations higher than 300 ppm were excluded from the dataset. R10 and Sy were applied as

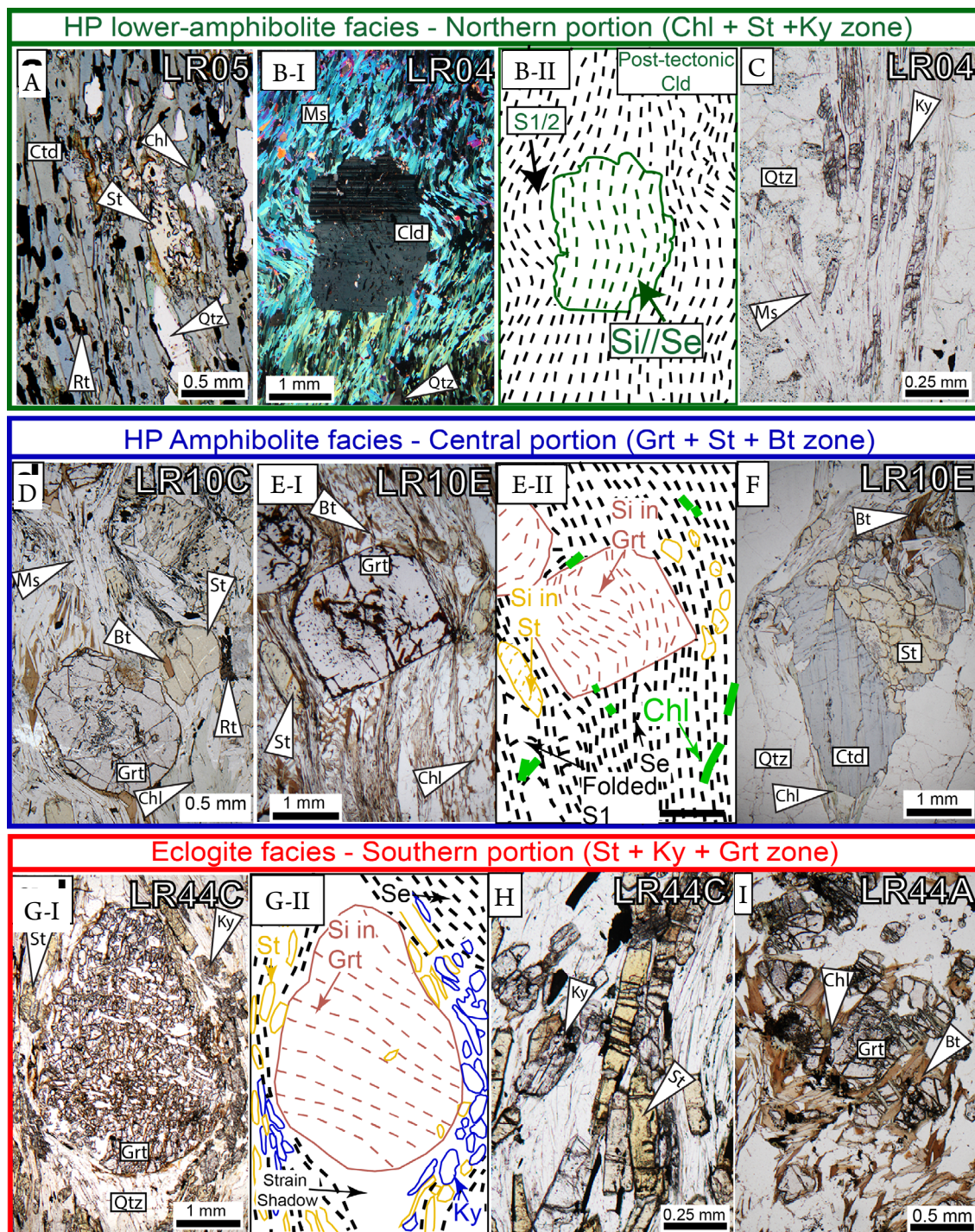


**Figure 2.** Representative transmitted light photomicrographs and schematic representations from thin section of studied metapelite. (A) Photomicrograph of staurolite and kyanite-bearing chlorite-chloritoid schist showing an anhedral staurolite crystal in chlorite matrix from the northern portion (plane polarized light) (Sample LR05). (B-I) Photomicrograph of chloritoid and kyanite-bearing muscovite schist showing the muscovite matrix and a porphyroblast of chloritoid (post-tectonic) from the northern portion (crossed polarized light) (Sample LR04). (B-II) Schematic representation of photomicrograph b, showing the slaty cleavage / fine grained schistosity S1/2 and the internal foliation in the post-tectonic chloritoid. (C) Photomicrograph of chloritoid and kyanite-bearing muscovite schist showing in detail the kyanite from the northern portion (plane polarized light) (Sample LR04). (D) Photomicrograph of staurolite and biotite-bearing garnet schist showing a porphyroblast of garnet and porphyroblasts of staurolite in a matrix of muscovite, biotite and quartz and a biotite included in staurolite from the central portion (plane polarized light) (Sample LR10C). (E-I) Photomicrograph of a staurolite-bearing garnet schist band showing a porphyroblast of garnet and porphyroblasts of staurolite in a matrix of muscovite, biotite and quartz from the central portion (plane polarized light) (Sample LR10E). (E-II) Schematic representation of microphotograph e-I showing the schistosity, the inclusion pattern in the garnet and staurolite and the random orientation of chlorite. (F) Photomicrograph of a staurolite and chloritoid-bearing garnet schist band showing a porphyroblast of chloritoid associated with staurolite from the central portion (plane polarized light) (Sample LR10E). (G-I) Photomicrograph of kyanite-bearing garnet-staurolite schist showing a porphyroblast of garnet and staurolite and kyanite in the matrix. Sample from the southern portion (plane polarized light) (Sample LR44C). (G-II) Schematic representation of photomicrograph g-I showing the continuous schistosity slightly deviated around garnet porphyroblast and the inclusions pattern in the garnet. (H) Photomicrograph of kyanite-bearing garnet-staurolite schist showing a porphyroblast of garnet surrounded by biotite and chlorite with random orientation. Sample from the southern portion (plane polarized light) (Sample LR44C). (I) Photomicrograph of kyanite-bearing staurolite schist showing retrograde biotite and chlorite in the border of the garnet (plane polarized light) (Sample LR44A). Abbreviations according to Kretz (1983). HP: high-pressure.

secondary standards to ensure the quality and reproducibility of the analyses (Luvizotto *et al.* 2009). Zr-in-rutile temperatures were calculated with the calibration of Tomkins *et al.* (2007).

Monazite dating (U-Th-Pb<sub>i</sub>) has been performed in LR10E and LR44C samples and followed the recommendations of Williams *et al.* (2006). A full thin section x-ray map (15 kV, 200 nA, 20–50 s dwell time and 30 µm electron beam size and step) was done for Ce and P to identify all monazite crystals and examine their textural relationships with other mineral phases. On the selected monazite crystals, high resolution compositional x-ray maps were carried out for Y, Al, Th, U, Pb, Si, Ca, Fe, La, and Ce (15 kV, 100 nA, 100 s dwell time and 10 µm electron beam size and step). X-ray maps collected for crystals from the same sample were processed together (*i.e.*, using the same color table for all crystals). Thus, concentration levels and zoning characteristics can be compared from crystal to crystal. The maps are then used to target distinctive domains for spot analyses and age calculations. Differently from the procedures highlighted by Williams *et al.* (2006), background measurements were performed for all analyses. Point analyses followed the method outlined by Vlach (2010), and the analytical conditions are presented in Table 2. Sample current values used for the analyses varied from 80 to 200 nA and

were constantly monitored to evaluate and avoid beam damage. Every 10 to 20 analyses on the unknowns were bracketed by three analyses on the Moacir monazite secondary standard to evaluate quality of the analyses. Spectral interference corrections (Th on U Mb and Th + Y on Pb Ma) were done offline and considered matrix correction factors. Interference corrections and age calculations were performed using the Age\_Cor program (Vlach 2010).

## LA-ICP-MS

Trace elements analyses in quartz were conducted through a New Wave NWR213 laser ablation system coupled to an Agilent 8800 triple quadrupole ICP-MS. The carrier gas was a He-Ar mixture. Helium gas carries the laser ablated sample aerosol from the sample cell, the He gas is mixed with Ar carrier gas and N to enhance sensitivity that flows into the ICP-MS torch. It was flushed through the ablation cup at 1 mL/min. A laser beam with diameter of 10 µm at laser energy of 6.7 J/cm<sup>2</sup> and a repetition rate of 4 Hz is used to ablate the sample. The signals were recorded over 60 seconds for each spot. The first 20 seconds were used to measure the background, while the next 30 ones were applied for acquiring the analysis

**Table 2.** Electron microprobe analysis (EPMA) conditions applied for the monazite trace element analysis.

Element	X-ray line	Crystal	CH	Acc.v	Peak Pos.	BG_L Pos.	BG_U Pos.	Peak (s)	BG (s)	High Volt.	Base Line	Window	Standard	Conc. Std. (%)	Curr. (A)	D.L. (ppm)
Y	La	TAP	1	15	70.048	1.25	1	100	50	1,635	3.5	3.2 (V)	Y <sub>2</sub> O <sub>3</sub> P&H	11.80	1.00E-07	110
Si	Ka	TAP	2	15	77.314	1.65	1.05	40	20	1,630	2.2	4.1 (V)	Wollastonite P&H	50.96	2.00E-08	60
Al	Ka	TAP	2	15	90.577	2.47	1.72	40	20	1,630	2.2	4.1 (V)	Al <sub>2</sub> O <sub>3</sub> P&H	99.99	2.00E-08	50
Th	Ma	PETJ	3	15	132.571	2	1.95	140	70	1,670	3.7	3.9 (V)	Th Glass MAC	5.90	1.00E-07	160
Ca	Ka	LIF	3	15	233.493	0.7	1.1	10	5	1,628	0.9	3.0 (V)	Apatite	54.02	2.00E-08	240
La	La	LIF	3	15	185.373	1.45	1.65	10	5	1,628	2.4	2.0 (V)	La <sub>2</sub> O <sub>3</sub> P&H	11.50	2.00E-08	1,200
Ce	La	LIF	3	15	178.132	1.45	1.65	10	5	1,628	2.3	2.0 (V)	CeO <sub>2</sub> P&H	11.90	2.00E-08	1,200
Pr	Lb	LIF	3	15	157.127	0.75	0.85	10	5	1,628	2.7	2.0 (V)	Pr <sub>6</sub> O <sub>11</sub> P&H	12.20	2.00E-08	1,600
Nd	Lb	LIF	3	15	150.713	0.9	1	10	5	1,628	2.3	2.0 (V)	Nd <sub>2</sub> O <sub>3</sub> P&H	11.80	2.00E-08	1,900
Sm	Lb	LIF	3	15	139.059	0.55	0.55	10	5	1,628	3.2	1.8 (V)	Sm <sub>2</sub> O <sub>3</sub> P&H	11.20	2.00E-08	1,800
Fe	Ka	LIF	3	15	134.693	0.75	0.65	10	5	1,628	2.4	3.1 (V)	Ilmenite MCS	35.03	2.00E-08	400
Gd	Lb	LIF	3	15	128.512	1	1	10	5	1,628	3.5	2.1 (V)	Gd <sub>2</sub> O <sub>3</sub> P&H	12.10	2.00E-08	1,800
Er	La	LIF	3	15	124.195	0.75	0	10	5	1,628	3.3	2.3 (V)	Er <sub>2</sub> O <sub>3</sub> P&H	11.90	2.00E-08	1,130
Tb	Lb	LIF	3	15	123.669	0.45	0	10	5	1,628	3.7	2.0 (V)	Tb <sub>2</sub> O <sub>3</sub> P&H	11.90	2.00E-08	2,200
Dy	Lb	LIF	3	15	119.035	0.65	0.55	10	5	1,628	3.7	2.3 (V)	Dy <sub>2</sub> O <sub>3</sub> P&H	12.00	2.00E-08	1,960
Yb	La	LIF	3	15	116.35	1.5	1.45	10	5	1,628	3	2.0 (V)	Yb <sub>2</sub> O <sub>3</sub> P&H	12.00	2.00E-08	1,430
U	Mb	PETL	4	15	118.932	3.98	3.98	300	150	1,670	3	2.7 (V)	UO <sub>2</sub> MAC	99.80	1.00E-07	65
S	Ka	PETL	4	15	172.02	-	2	10	5	1,670	3	2.5 (V)	PbS P&H	33.46	2.00E-07	160
P	Ka	PETH	5	15	197.105	2.1	2.65	10	5	1,686	1.7	3.0 (V)	Apatite	40.78	2.00E-08	150
Pb	Ma	PETH	5	15	169.251	3.65	4.2	300	150	1,686	1.8	3.0 (V)	PbS P&H	93.29	2.00E-07	40

CH: Spectrometer Chanel; Acc. V: Acceleration voltage; Peak Pos.: Peak position in mm; BG\_L Pos.: Lower background position in mm from the peak; BG\_U Pos.: Upper background position in mm from the peak; Peak (s): counting time on peak position in s; BG (s): Counting time on each background (upper and lower) position in s; Conc. Stds (%): Concentration of the element in the standard; Curr. A: Current of standard analyses in A; D.L.: Minimum detection limit (3 sigma) for the unknowns; MAC: Micro-Analysis Consultants Ltd. P and H Developments Ltd.

signal and the last 10 seconds were used for system wash out. The following isotopes were analyzed:  $^7\text{Li}$ ,  $^{27}\text{Al}$ ,  $^{29}\text{Si}$ ,  $^{48}\text{Ti}$ ,  $^{49}\text{Ti}$ ,  $^{57}\text{Fe}$ , and  $^{72}\text{Ge}$ . Ti concentrations were calculated using  $^{49}\text{Ti}$  to avoid the isobaric interference from  $^{48}\text{Ca}$  (present in most well characterized reference glasses) on  $^{48}\text{Ti}$ . The SRM 610 was used as the calibration standard. Ti-in-Quartz temperatures were calculated using the calibration of Thomas *et al.* (2010).

## SAMPLE DESCRIPTIONS: MICROSTRUCTURES AND MINERAL ASSEMBLAGES

In the following descriptions and throughout the text, the metapelitic rocks from Campestre Formation are grouped according to their geographical distribution and mineral assemblages. In all results and discussion, quartz and muscovite are omitted from mineral assemblages, as they are excessive phases. A fluid rich in  $\text{H}_2\text{O}$  was also in excess and present during the metamorphism. A summary of mineral chemistry of the samples is further presented. A detailed description of the mineral chemistry of the studied rocks can be found in Fumes *et al.* (2017).

### High-pressure lower amphibolite facies: Northern portion of the Luminárias Nappe (LR04, LR50 and LR05 samples)

Staurolite and kyanite-bearing chlorite-chloritoid schist; and chloritoid and kyanite-bearing muscovite schist are the metapelitic rocks from the northern portion (Fumes 2017). In both rocks, the  $S_{1/2}$  foliation is a slaty cleavage/fine-grained schistosity and its texture is lepidoblastic.

The continuous schistosity of the staurolite and kyanite-bearing chlorite chloritoid schist (sample LR05) is defined by chloritoid, chlorite, quartz, muscovite, rutile, staurolite, kyanite, ilmenite, zircon, and apatite (Fig. 2A). Staurolite only occurs as anhedral crystals with rims replaced by chlorite (Fig. 2A). Chlorite also occurs as anhedral crystals and they are always associated with the chloritoid crystals (Fig. 2A).

In the chloritoid and kyanite-bearing muscovite schist (LR04 and LR50 samples), the rock matrix is composed of muscovite, quartz, kyanite, ilmenite, rutile, zircon, and chlorite (Figs. 2B and 2C). The foliation is slightly crenulated according to  $F_3$  microfolds. Chloritoid occurs as porphyroblasts, with abundant inclusions of quartz, ilmenite and rutile, which are orientated parallel to main foliation  $S_{1/2}$ . Based on their microstructural relationship, main cleavage overgrowing, and absence of strain shadows, chloritoid porphyroblasts are interpreted as post-tectonic to the main foliation  $S_{1/2}$  (Fig. 2B). The average formula of the chloritoid porphyroblasts is  $\text{Fe}^{+2}_{0.77}\text{Mg}_{0.16}\text{Mn}_{0.05}\text{Al}_{1.95}\text{Fe}^{+3}_{0.07}\text{Si}_{0.99}\text{O}_5(\text{OH})_2$  with  $X_{\text{Fe}}$  (Fe/Fe + Mg) ratio between 0.81-0.87. Chlorite average formula is  $\text{Mg}_{2.02}\text{Fe}^{2+}_{2.43}\text{Mn}_{0.05}\text{Si}_{2.51}\text{Al}_{2.94}\text{Fe}^{3+}_{0.02}\text{Na}_{0.01}\text{O}_{10}(\text{OH})_{16}$  and  $X_{\text{Fe}}$  ranges between 0.51 and 0.59.

The peak metamorphic assemblage in the northern portion is represented by  $\text{Chl} + \text{Ky} + \text{St} + \text{Rt}$ , under high-pressure lower amphibolite facies conditions. As chloritoid in LR04 sample is post-tectonic to  $S_{1/2}$  (Fig. 2B), it is interpreted as a

retrograde phase, which is not present in the peak metamorphic assemblage.

### High pressure amphibolite facies: Central portion of the Luminárias Nappe (LR10C and LR10E samples)

In the central portion, the main rock type is a staurolite-biotite-garnet muscovite schist (LR10C sample, Fig. 2D), in which muscovite, biotite and quartz define the main and homogeneous schistosity ( $S_{1/2}$ ). Ilmenite, zircon, monazite, and rutile occur as accessory minerals and follow the main foliation fabric. Garnet porphyroblasts range from 1 to 5 mm in diameter, whereas staurolite varies from 1 to 2.5 mm in length. Both porphyroblasts contain abundant inclusions of quartz, monazite, ilmenite, and tourmaline. Biotite crystals occur oriented along the  $S_{1/2}$  foliation, in contact with garnet as well as included in staurolite. This texture indicates that biotite is in equilibrium with garnet and staurolite (Figs. 2D and 2E). Furthermore, garnet and staurolite are interpreted as syntectonic associated with  $D_{1/2}$ , because their inclusion patterns are rotated and curved (Fig. 2D). Therefore, the peak metamorphic assemblage in the central portion is  $\text{Bt} + \text{St} + \text{Grt} + \text{Rt}$ , which is stable under amphibolite facies conditions. Chlorite occurs as a retrograde phase at garnet and staurolite rims, as well as replacing biotite. Chlorite does not follow the main foliation (Fig. 2D).

LR10E sample is from the same outcrop as the LR10C sample, but this one is banded with distinct mineral assemblages in each band. One band is composed of garnet, muscovite, staurolite, and quartz (Fig. 2E), whereas the other comprises chloritoid, staurolite, quartz, muscovite and biotite (Fig. 2F). In both bands, ilmenite, rutile, monazite and zircon are accessory minerals and chlorite occurs as a retrograde phase (Fig. 2E). Garnet, chloritoid and staurolite are porphyroblasts, with average diameter of 2.0, 1.5 and 1.0 mm, respectively. The foliation is defined by the preferred orientation of muscovite, biotite, staurolite and quartz and is classified as a fine-grained schistosity ( $S_{1/2}$ ). Garnet and staurolite porphyroblasts have inclusions of ilmenite, quartz, and tourmaline. Both staurolite and garnet porphyroblasts are interpreted as syntectonic to  $S_{1/2}$  based on the inclusion pattern that indicates rotation and on the continuity of the internal foliation defined by inclusions (Si) and external foliation ( $\text{Se} // S_{1/2}$ ). Chloritoid porphyroblasts with corroded rims are associated with euhedral staurolite (Fig. 2F) and are interpreted as pre-tectonic to  $S_{1/2}$ . The compositional banding and the mineral assemblages described above indicate that the equilibrium was only attained within the same compositional band. Although mineral phases from both compositional bands may have coexisted in different domains in the rock, they are not necessarily in equilibrium with each other. Since LR10C sample has a relatively homogeneous composition (*i.e.*, it is not banded), it is taken as a representative sample of the central portion of Luminárias Nappe.

In the central portion of Luminárias Nappe, the garnet porphyroblasts are intensely zoned with higher content of

grossular and spessartine in the core, whereas almandine and pyrope increase towards the rims. Garnet formula is  $Fe^{2+}_{2.2-2.6} Mn_{0-0.2} Mg_{0.2-0.4} Ca_{0.2-0.5} Ti_{0-0.3} Fe^{3+}_{0-0.2} Al_{1.9-2} Si_{2.8-3} O_{12}$ , and the medium  $X_{Fe}$  has almost no variation from core to rim, from 0.86 to 0.87. The average formula of the staurolite in this sample is  $Fe^{+2}_{3.18} Mg_{0.55} Mn_{0.01} Ti_{0.12} Cr_{0.01} Al_{17.70} Si_{7.72} O_{46.5} H_3$ , with  $X_{Fe}$  medium of 0.85 (0.84–0.86) and Zn content varying from 0.05 to 0.13 a.p.f.u. (a for atoms, p for per, f for formula and u for unit). Biotite has 0.08 a.p.f.u. of Ti and  $X_{Fe}$  is 0.51. Muscovite has  $X_{Fe}$  0.47.

Monazite is observed in all samples from the central portion. This mineral occurs in the matrix and included in garnet, staurolite, and rutile. In LR10A sample, like LR10C, rounded crystals of allanite occur associated with anhedral monazite crystals (Fig. 3).

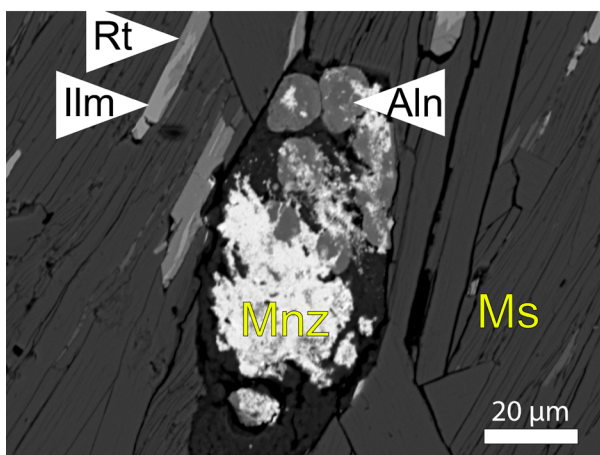


**Figure 3.** Back-scattered electron (BSE) image from LR10A sample showing a monazite associated with circular allanite crystals in the rock matrix.

### Eclogite facies: southern portion of the Luminárias Nappe (LR44C and LR44A Samples)

Southern portion rocks are represented by sample LR44C, a garnet-staurolite schist, in which the matrix is composed of staurolite, muscovite, quartz, kyanite, rutile, ilmenite, zircon, monazite, and garnet. The latter occurs as porphyroblasts with inclusions of quartz, staurolite, ilmenite, monazite, and rutile (Fig. 2G). Oblique internal inclusions and strain shadows indicate that the garnet porphyroblasts are syntectonic to  $S_{1/2}$ . The continuous schistosity is defined by preferred orientation of staurolite, quartz, and kyanite. Kyanite crystals are often observed associated with staurolite (Fig. 2H), which indicate equilibrium between the two minerals. Therefore, textural relationships show that the metamorphic peak assemblage is  $St + Ky + Grt + Rt$ , a high pressure, amphibolite to eclogite facies assemblage. Biotite and chlorite are interpreted as retrograde phases, since both minerals occur with random orientation in the matrix or at the garnet rims (Fig. 2I).

Garnet porphyroblasts from the southern portion are also zoned with representative formula of  $Fe^{2+}_{1.6-2.5} Mn_{0-0.6} Mg_{0.1-1.2} Ca_{0-0.5} Ti_{0-0.8} Fe^{3+}_{0-0.8} Al_{1.8-2} Si_{2.6-3} O_{12}$ ; in the cores,  $X_{Fe}$  is 0.90, and in rims, it is 0.89. Garnet cores present higher content of spessartite and lower almandine percentages, whereas pyrope and grossular maintain constant concentrations along sections through all the garnet crystals. Staurolite average composition is  $Fe^{+2}_{3.18} Mg_{0.59} Mn_{0.03} Ti_{0.13} Cr_{0.01} Al_{17.59} Si_{7.77} O_{46.3} H_3$  with  $X_{Fe}$  of 0.84 and Zn content varies from 0.01 and 0.03 a.p.f.u. The  $X_{Fe}$  of the muscovite is 0.44.

### P-T PSEUDOSECTION

P-T pseudosections calculated for LR10C (amphibolite facies, central portion) and LR44C (eclogite facies, southern portion) samples are presented in Figure 4. Whole rock

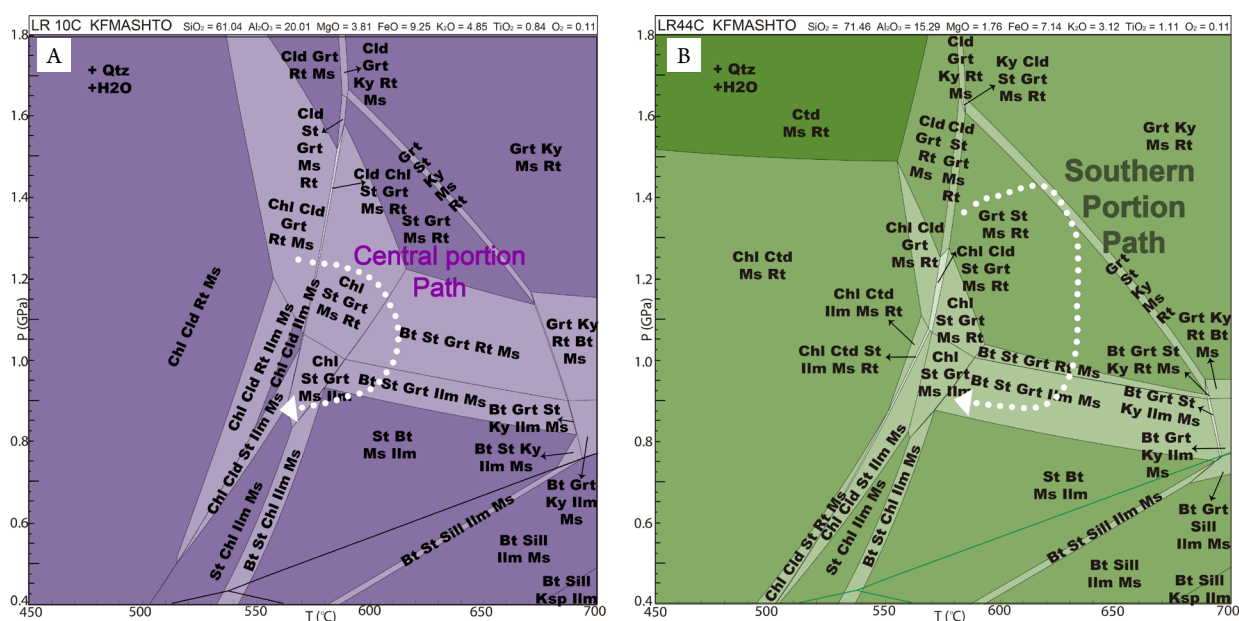


**Figure 4.** Pressure-Temperature (P-T) pseudosections for the Luminárias Nappe from the bulk compositions (presented on top of the diagram in molar proportion) calculated for the KFMASHTO model chemical system. The arrow indicates the P-T-t paths. (A) P-T pseudosection for sample LR10C (central portion of the Luminárias Nappe). (B) P-T pseudosection for sample LR44C (southern portion of the Luminárias Nappe).

chemical composition (in molar proportion) is presented in Figure 4. The projection is in the system KFMASH<sub>TO</sub>, and the minerals involved in the calculations are quartz, muscovite, garnet, chloritoid, staurolite, ilmenite, rutile, chlorite, kyanite, sillimanite, K-feldspar, and water. Quartz and muscovite are ubiquitous in the studied rocks and metamorphism took place under *sub-solidus* *P-T* conditions. Therefore, quartz, muscovite, and water were set to be in excess. The two *P-T* pseudosections (LR10C and LR44C samples) have similar topology and were calculated between 0.4–1.8 GPa and 450–700°C (Figs. 4A and 4B). In both diagrams, the chloritoid stability is exclusively controlled by temperature, and the mineral is stable at temperatures below 590°C. The occurrence of chlorite is also controlled by temperature. In the pseudosection calculated for LR10C sample, chlorite happens along all the *P* range and in *T* lower than 615°C. In the pseudosection calculated for LR44C sample, chlorite occurs under *P* conditions lower than 1.4 GPa and *T* in lower than 580°C. For both samples, staurolite occurs in *T* between 505 and 690°C and *P* in lower than 1.7 GPa. Garnet is stable in *P* higher than 0.8 GPa and *T* higher than 490°C in the pseudosection of the LR10C sample and 555°C in the pseudosection of LR44C sample. Biotite occurs at *P* lower than 1.1 GPa and at *T* higher than 480°C in the pseudosection of LR10C sample and 530°C in the pseudosection of LR44C sample. Kyanite and sillimanite are the aluminum silicates that appear in pseudosections within the investigated *P-T* range. Kyanite is stable at *T* higher than 580°C and *P* higher than 0.8 GPa, whereas sillimanite is only stable at *P* lower than 0.8 GPa and *T* higher than 580°C. Ilmenite and rutile are the Ti-bearing phases, the former is stable at *P* lower

than 1.0 GPa and *T* lower than 500°C and the latter is only stable in conditions of *P* higher than 1.0 GPa and *T* higher than 500°C. Muscovite, quartz, and water are stable and appear in almost all the fields, apart from a small *P-T* field at *T* higher than 575°C and *P* lower than 0.5 GPa, where the K-feldspar is stable, instead of the muscovite.

According to the calculated pseudosections (Fig. 4), the mineral peak assemblage of the central portion of Luminárias Nappe (St + Bt + Grt + Rt, abbreviations according to Kretz 1983) is stable from 590 to 685°C and from 0.9 to 1.2 GPa. The mineral peak assemblage that represents the southern portion of the Luminárias Nappe (St + Ky + Grt + Rt) occurs in a tight diagonal field and is stable from 585 to 690°C and from 0.9 to 1.65 GPa, which corresponds to high pressure amphibolite — eclogite facies transition.

## SINGLE ELEMENT THERMOBAROMETRY

Single element thermobarometry is applied as an independent technique to constrain the metamorphic peak. The geothermometers applied in this study are Zr-in-rutile and Ti-in-quartz, and both are suitable to be applied here since all rocks contain quartz, zircon and rutile in excess.

## Trace elements in rutile and quartz

Rutile crystals from five samples, LR04, LR05, LR10C, LR10E and LR44C, were analyzed. Data from the trace elements in rutile obtained for all the studied samples are presented in Table 3 and Figures 5 and 6.

**Table 3.** Trace element composition (in ppm) of the analyzed rutile from LR04, LR05, LR10C and LR44C samples.

Sample	DL Spot	Texture	25 20 40 50 85 45 40							P (Gpa)	T (°C)	T (°C) +	T (°C) -	RSE in ppm						
			Si	Al	Fe	Cr	Ta	Zr	Nb					Si	Al	Fe	Cr	Ta	Zr	Nb
LR04	Rt1-1	Mtx	108	191	9,662	1,478	BD	BD	1,573					3	3	19	8			9
LR04	Rt1-2*	Mtx	159	275	10,649	1,492	254	89	11,345	0.9	557	5	6	3	3	20	8	14	8	16
LR04	Rt2	Mtx	93	228	10,097	1,752	328	104	12,163	0.9	567	5	5	3	3	19	8	14	7	17
LR04	Rt3	Mtx	BD	90	12,864	1,444	180	96	11,646	0.9	563	5	5	3	22	8	14	8	16	
LR04	Rt4	Mtx	136	254	11,683	1,512	532	126	12,904	0.9	581	4	4	3	3	21	8	14	8	17
LR04	Rt5	Mtx	215	619	8,807	814	303	148	5,746	0.9	592	4	4	3	3	18	7	14	8	13
LR04	Rt7	Mtx	276	365	9,880	972	262	126	6,585	0.9	581	4	4	3	3	20	7	14	8	13
LR04	Rt8	Mtx	238	614	9,678	958	BD	89	7,606	0.9	557	5	6	3	3	19	7		7	14
LR04	Rt9C	Mtx	266	714	9,685	1,019	BD	81	4,530	0.9	552	6	6	3	3	19	7		8	12
LR04	Rt9D	Mtx	252	656	8,714	931	98	104	4,292	0.9	567	5	5	3	3	18	7	15	8	11
LR04	Rt9E	Mtx	299	794	8,550	978	BD	111	4,257	0.9	572	5	5	3	3	18	7		8	11
LR04	Rt11	Mtx	89	212	6,475	445	BD	104	1,482	0.9	567	5	5	3	3	16	6		7	9
LR04	Rt13	Mtx	178	524	5,519	855	BD	133	2,922	0.9	585	4	4	3	3	15	7		7	10
LR05	Rt1-1*	Mtx	192	418	8,434	1,505	BD	BD	10,723					3	3	19	8			16
LR05	Rt1-2	Mtx	206	429	5,395	1,266	BD	BD	3,083					3	3	15	8			10
LR05	Rt6	Mtx	252	656	5,503	978	BD	BD	BD					3	3	15	7			
LR05	Rt7	Mtx	220	614	5,348	BD	BD	BD	98					3	3					7
LR05	Rt8	Mtx	229	566	9,079	828	106	BD	11,408					3	3	19	7			16

Continue...

Table 3. Continuation.

Sample	DL Spot	Texture	25	20	40	50	85	45	40	P (Gpa)	T (°C)	T (°C) +	T (°C) -	RSE in ppm											
			Si	Al	Fe	Cr	Ta	Zr	Nb					Si	Al	Fe	Cr	Ta	Zr	Nb					
LR05	Rt9	Mtx	187	572	5,690	657	BD	BD	BD					3	3	15	7								
LR05	Rt10	Mtx	271	175	7,921	1,273	BD	52	5,564	0.9	523	7	8	3	3	17	8			6	12				
LR10C	Rt3	Mtx	210	217	2,293	62	BD	141	1,510	1.1	597	3	3	3	3	12	5			6	7				
LR10C	Rt4	Mtx	266	307	2,371	BD	131	104	881	1.1	575	4	4	3	3		4	12	6	6					
LR10C	Rt10	Mtx	131	228	2,130	BD	106	74	993	1.1	553	5	5	3	3		4	12	6	7					
LR10E	Rt1-1*	Mtx	98	262	4,229	BD	BD	149	912	1.1	601	13	15	12	11					28	36				
LR10E	Rt1-2	Mtx	125	131	3,893	BD	BD	99	1,211	1.1	572	17	21	12	11					27	37				
LR10E	Rt7	Mtx	227	327	1,725	BD	BD	149	1,180	1.1	601	13	15	12	11					28	37				
LR44C	Rt68-1*	Mtx	159	206	1,119	62	BD	BD	1,342					11	8	29	17								32
LR44C	Rt68-2	Mtx	257	487	1,422	89	BD	BD	1,797					11	9	30	17								35
LR44C	Rt65-1*	Incl. Grt	28	450	7,758	554	1,679	192	12,960	1.4	632	8	9	10	9	51	19	53	21	66					
LR44C	Rt65-2	Incl. Grt	BD	413	7,128	506	1,032	163	11,583	1.4	619	9	10		9	49	19	52	21	64					
LR44C	4_Rt1_1*	Mtx	89	196	1,158	62	BD	BD	762					10	8	29	18								30
LR44C	4_Rt1_2	Mtx	65	127	1,998	BD	BD	BD	426					10	8		16								28
LR44C	4_Rt1_3	Mtx	28	79	941	BD	BD	BD	510					10	8		17								29
LR44C	5_Rt1_1*	Mtx	84	318	1,283	62	BD	BD	643					10	9	30	16								29
LR44C	5_Rt1_2	Mtx	51	106	1,026	BD	BD	BD	1,070					10	8		16								31
LR44C	6_Rt1_1*	Mtx	BD	69	715	BD	BD	BD	419						8		19								28
LR44C	6_Rt1_2	Mtx	BD	58	490	BD	BD	BD	482						7		17								28
LR44C	6_Rt1_3	Mtx	BD	64	575	55	BD	BD	615						7	26	17								29
LR44C	7_Rt1_1	Incl. Grt	28	111	5,099	335	BD	185	3,230	1.4	629	8	9	11	8	43	18			21	40				
LR44C	7_Rt2_1	Incl. Grt	70	228	8,955	643	786	192	9,863	1.4	632	8	9	10	8	54	20	51	21	59					
LR44C	7B_Rt1_1*	Incl. Grt	28	238	6,654	561	647	192	7,494	1.4	632	8	9	9	8	48	19	51	21	53					
LR44C	7B_Rt1_2	Incl. Grt	BD	222	6,452	547	197	170	7,361	1.4	623	9	10		8	47	19	50	21	53					
LR44C	8_Rt1_1	Incl. Grt	BD	233	6,459	554	213	178	7,361	1.4	626	8	9		8	48	19	49	20	53					
LR44C	3_Rt1_1	Mtx	28	48	466	BD	BD	BD	1,685					11	7		17								34
LR44C	3_Rt1_2*	Mtx	BD	BD	513	BD	82	BD	1,251								15	50							32
LR44C	Rt1(mount)	Incl. Grt	52	267	11,124	493	BD	170	14,362	1.4	622	11	13	12	11	60	37			28	80				

DL: 2 sigma minimum detection limit (in ppm); RSE: Relative standard errors from counting statistics (2 sigma); T (Temperature) is calculated using equation of Tomkins *et al.* (2007); P (Pressure) estimate based on the pseudosection; \*: data plotted in Figure 5 (grains with more than 1 spot); T (°C) + and T (°C) -: errors in temperature calculated based on the RSE; BD: below detection limit.

In LR04 and LR05 samples, from the northern portion of Luminárias Nappe (high pressure lower amphibolite facies mineral assemblage, since the mineral peak assemblage is chlorite + kyanite + staurolite + muscovite + quartz + rutile), rutile is abundant and occurs as subhedral crystals in the matrix. Most rutile crystals contain ilmenite needles and zircon inclusions (Figs. 5A, 5B and 5C).

In LR10C and LR10E samples, from the central portion (high-pressure amphibolite facies mineral assemblage), rutile is rare, has anhedral shape and is frequently associated with ilmenite in a texture indicating that the latter replaces rutile

(Fig. 5E). Rutile does not occur as inclusion in garnet, and several crystals have zircon inclusions. Due to the characteristics described above, only 6 out of 23 analyses of LR10C and LR10E samples passed adopted quality control, that is, Si content below 300 ppm.

In LR44C sample, from the southern portion (eclogite facies mineral assemblage), rutile crystals are mostly free of inclusions, although sometimes a few ilmenite needles and zircon inclusions are observed. Rutile crystals have subhedral shape and occur either in the matrix or as inclusion in garnet (Fig. 5D).

Rutile crystals from the northern portion samples (LR04 and LR05) have similar composition of trace elements and present the highest content of Nb (several rutile crystals from sample LR44C also have high Nb content), Fe, Al and Cr among all the studied samples (Tab. 3 and Fig. 6). High values of Nb are not followed by Ta. The average Zr concentration is the lowest among the studied samples, although maximum (148 ppm, LR04) and minimum (52 ppm, LR05) values are like those of LR10C and LR10E samples. It is noteworthy that Zr was below the EPMA detection limit (45 ppm) in one analysis of LR04 sample and six analyses of LR05 sample.

In the central portion samples (LR10C and LR10E), rutile crystals have the lowest content of Nb, Fe, Cr and Ta among the studied samples (Tab. 3 and Fig. 6). Al content is similar to LR44C sample. As presented above, maximum (149 ppm, LR10E) and minimum (74 ppm, LR10C) Zr content in rutile from LR10C and LR10E samples are like those of LR04 and LR05 samples, although the average is higher.

Differently from the other samples, rutile occurs as an inclusion in garnet and in the matrix in LR44C sample (southern portion). Crystals from the two textural contexts have distinct composition of trace elements. Those crystals included

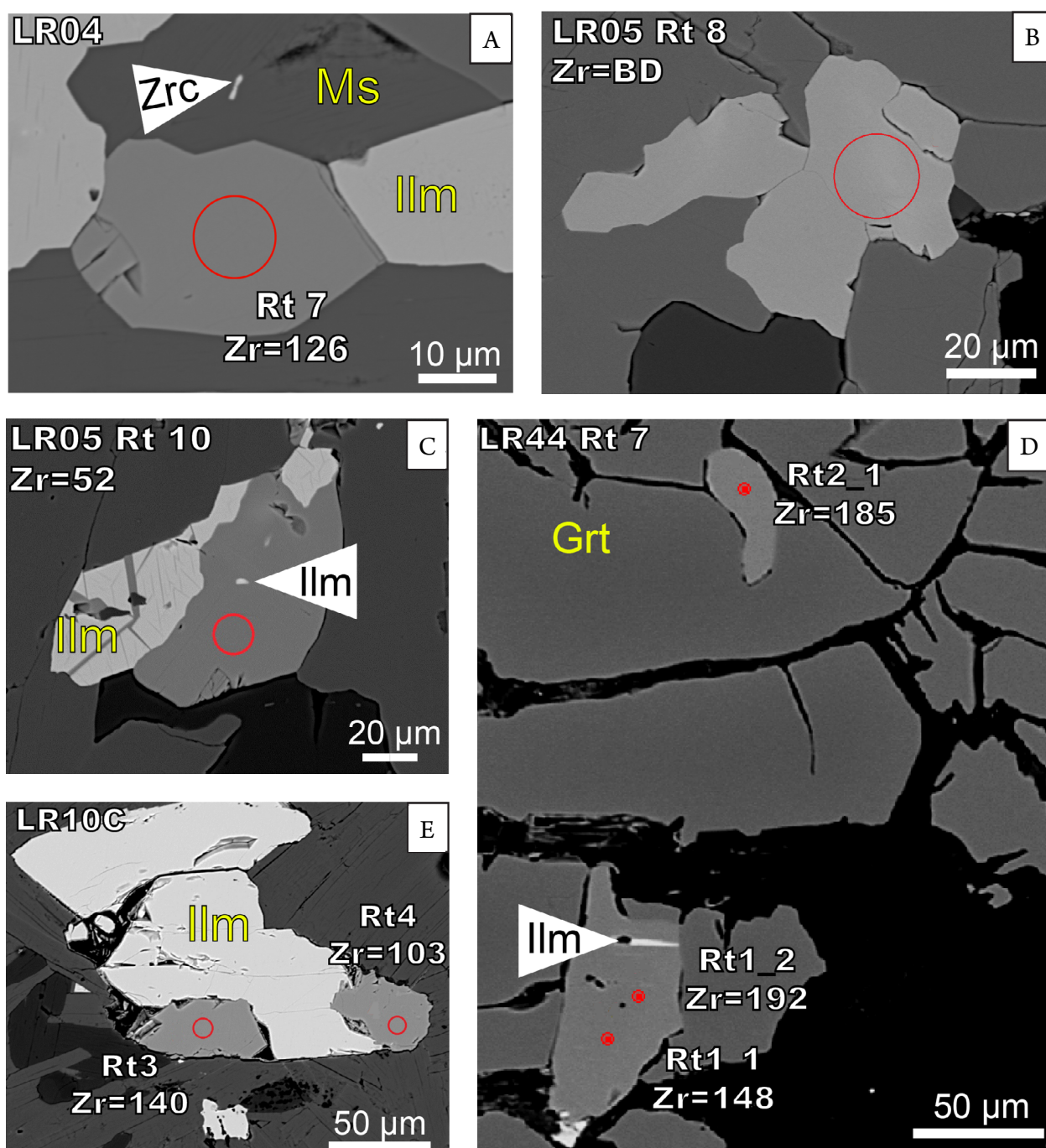


**Figure 5.** Back-scattered electron (BSE) images of representative rutile grains with concentrations of Zr (in ppm). (A) Rutile (Rt7) from LR04 sample (northern portion). (B) Rutile (Rt8) from the LR05 sample (northern portion). (C) Rutile (Rt10) from the LR05 sample (northern portion) with ilmenite inclusion and ilmenite lamella. (D) Rutile (Rt7) from LR44C sample (southern portion) included in garnet. Ilmenite lamella is observed in a grain. (E) Rutiles (Rt3 and Rt4) from LR10C (northern portion) sample associate with ilmenite. Red circles indicate position of the analyzed spots. Grains are labelled according Table 2.

in garnet have the highest content of all trace elements when compared to those from the matrix. All analyses of Ta and Zr are below the EPMA detection limit (85 and 45 ppm, respectively) for matrix rutile. Zr content in included rutile crystals from LR44C sample is the highest among all analyzed samples, with average of 159 ppm and maximum concentration of 192 ppm.

Quartz trace element concentrations were measured by LA-ICP-MS from LR44C sample, southern portion (Tab. 4). Only the quartz from this sample was analyzed because Zr-in-rutile content shows a small spread and the sample is from the higher metamorphic conditions of the Luminárias Nappe. Ti content ranges from 6.6 to 11.3 ppm.

### Temperature calculations

Isopleths for the Zr-in-rutile (Tomkins *et al.* 2007) and the Ti-in-quartz (calibration of Thomas *et al.* 2010) geothermometers are presented in Figure 7. Since both geothermometers are pressure-dependent, it is crucial to have a pressure estimation to calculate temperature. However, if both Zr-in-rutile and Ti-in-quartz geothermometers are applied for the same sample, equilibrium pressure and temperature conditions are given by the crossing of the isopleths in *P-T* space. According to Tomkins *et al.* (2007), a conservative estimation of temperature is given by the upper end of the box-plot box (third quartile). Temperatures presented herein are calculated according to this recommendation.

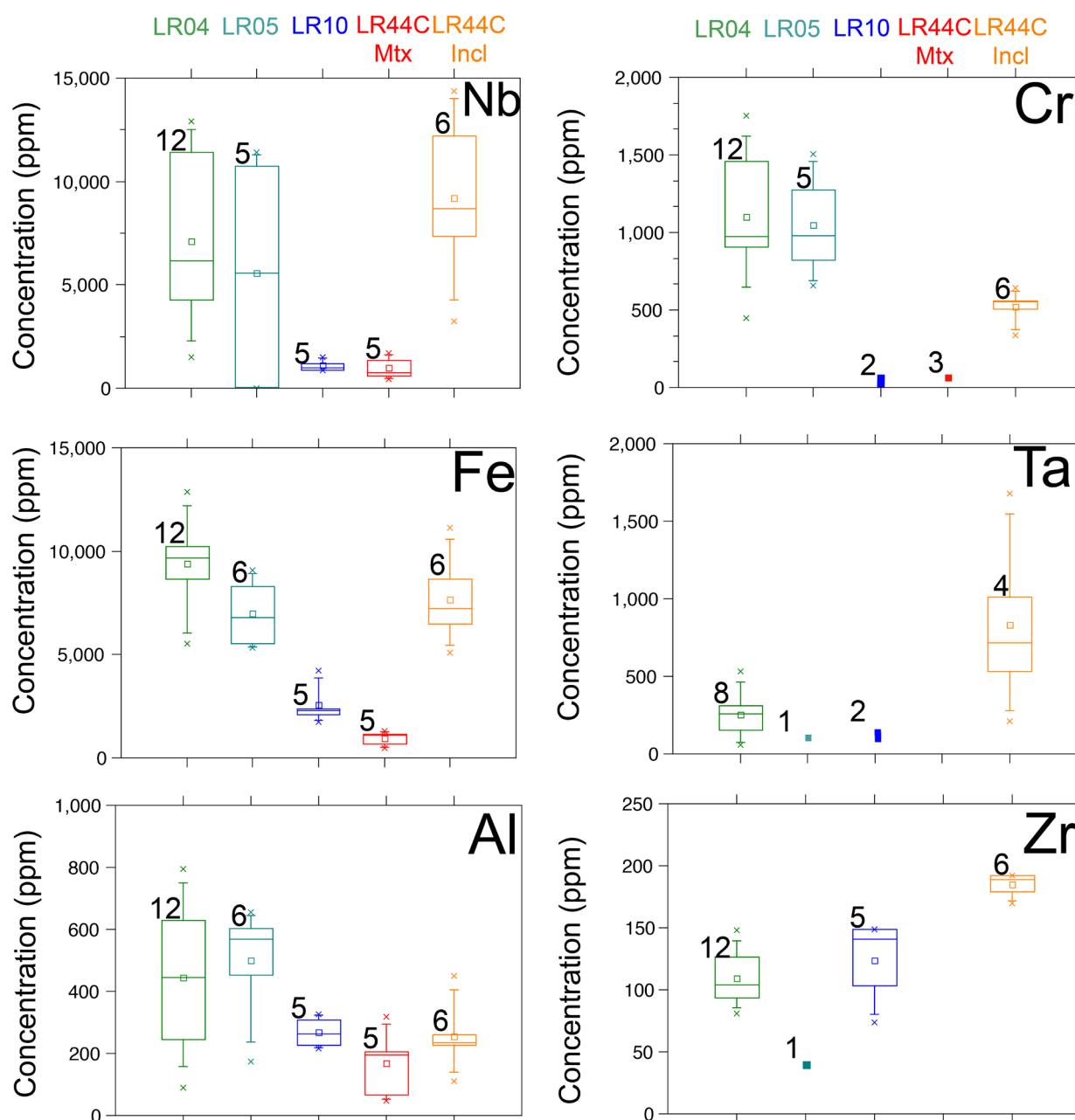


**Figure 6.** Boxplots showing concentration (in ppm) of the trace elements (Nb, Cr, Fe, Ta, Al and Zr) in rutile crystals from studied samples. In LR44C sample data from matrix rutile (Mtx) and included in garnet rutile crystals (Incl) are individualized. Whiskers represent the 5th and 95th percentile. Boxes represent the second (bottom-25%) and third quartile (top-75%). The square and bar inside the boxes represent the average and the media, respectively. The numbers on top of each box represent the number of analyses that are showed in the graph. When the numbers of analyses above detection limits are equal or lower than three only the value of the analyzed spots are plotted (solid squares). Only analyses above the minimum detection limit are presented.

Taking into account the stability field for the peak assemblage (Bt + St + Grt + Rt) in LR10C and LR10E samples (Fig. 4) and the Zr-in-rutile isopleths (Fig. 7B), the results indicate only the highest concentration of Zr plot in the stability field, defining a pressure range from 1.0 to 1.1 GPa. For this pressure range, temperatures calculated for the third quartile content (149 ppm) are  $597 \pm 3$  and  $601 \pm 15^\circ\text{C}$ , respectively.

For LR44C sample, the Zr-in-rutile and Ti-in-quartz isopleths intercept each other at ca.  $630 \pm 13^\circ\text{C}$  and 1.4 GPa (third quartile values for both elements). These results are in compliance with the stability field for the peak assemblage of the rock (Grt + St + Ky + Rt — Fig. 7).

For the northern portion, high pressure lower amphibolite facies conditions are constrained by the peak mineral assemblage Chl + Ky + St + Rt. This occurs along a wide pressure window (see KFMASH petrogenic grid in White *et al.* 2014). However, since results for LR10C/E and LR44C confirm that the metamorphic conditions decrease to the north, an estimated pressure of 0.9 GPa was used to calculate Zr-in-rutile temperatures for the northern portion. For LR04 sample, the calculated temperature is  $580 \pm 4^\circ\text{C}$  (125 ppm — third quartile).

### MONAZITE GEOCHRONOLOGY

U-Th-Pb<sub>T</sub> monazite dating was carried out in samples of the central (LR10E) and southern (LR44C) portions and comprised crystals from the rock matrix, as well as included in garnet, staurolite, kyanite, and rutile. Major and trace elements analyses, as well as compositional maps of 32 crystals were carried out (Fig. 8 and Tab. 5).

A compositional zoning of Y, Th, Pb and U is observed in several monazite crystals (Fig. 8), but it has no effect on the calculated ages. Systematic variations on the mean ages are linked to textural monazite settings in LR10E sample, in which monazite crystals included in garnet and staurolite present older ages ( $615 \pm 6$  Ma) when compared to those in the matrix ( $600 \pm 8$  Ma) (Fig. 9 and Tab. 6). In LR44C sample, results for matrix and included monazites crystals (in garnet, staurolite, kyanite and rutile) are indistinguishable, and the mean age is  $632 \pm 4$  Ma. Monazite crystals from LR44C sample have the highest content of Y among all the analyzed samples (Fig. 10).

Allanite occurs associated with the monazite in LR10A sample (Fig. 3). All monazite analyses in this sample were discarded due to the low total (sum of all analyzed elements) and no coherent U-Th-Pb<sub>T</sub> ages. Although the analyses are not used in further discussion, the presence of allanite replacing monazite is useful to establish the metamorphic P-T path that is further discussed.

### DISCUSSION

#### Metamorphic conditions and P-T paths

In the present study, the metamorphic gradient that has been previously described for the Luminárias Nappe region (Trouw *et al.* 1980, Ribeiro & Heilbron 1982, Peternel *et al.* 2005, Trouw *et al.* 2000, Silva 2010) is characterized based on peak metamorphic mineral assemblage, pseudosection modeling and geothermometry of trace elements. It is the first attempt to quantify, by a multi-method approach, the peak metamorphic conditions of the studied rocks. Furthermore, P-T paths

**Table 4.** Trace element composition of analyzed quartz from LR44C sample. Concentrations are in ppm. Temperature calculations are after the calibration of Thomas *et al.* (2010), using 1.4 GPa.

Spot #	Li	Al	Ti	Fe	Ge	T (°C)	T (°C) +	T (°C) -	RSE-Al	RSE-Ti	RSE-Fe
128	< 12.64	75.20	11.30	< 14.23	< 1.59	631	22	29	2.53	3.51	
130	< 12.07	27.11	6.61	< 12.79	< 1.56	590	26	37	1.80	2.70	
131	< 12.72	46.39	10.75	51.0	< 1.61	627	17	20	1.72	2.47	< 19.19
132	< 12.17	69.60	9.33	94.0	< 1.40	616	19	23	1.92	2.48	< 17.53
133	< 15.62	24.61	6.84	< 15.91	< 2.00	593	27	40	1.99	2.99	

RSE: Relative Standard Errors from counting statistics (2 sigma) in ppm (only shown for analyses above the detection limit). T (°C) + and T (°C) -: errors in temperature calculated based on the RSE, BD: below detection limit.

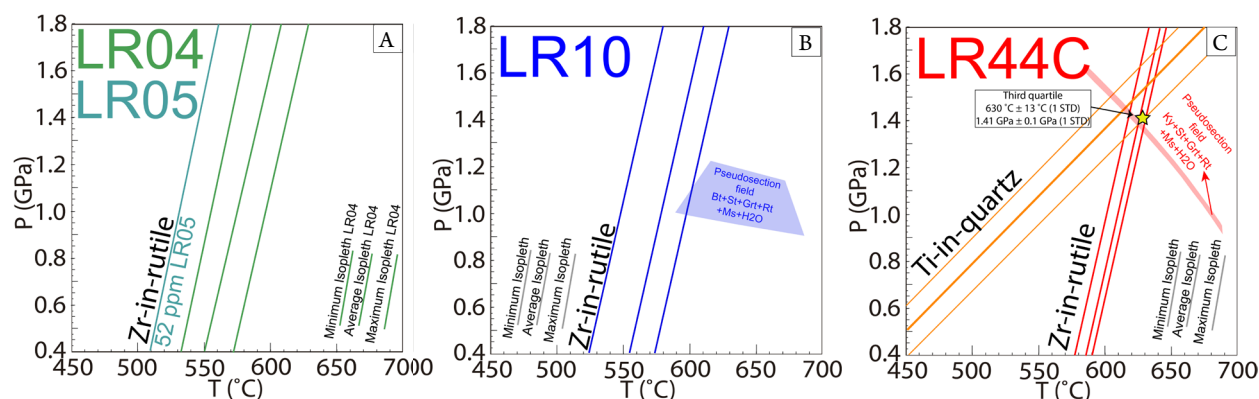


**Figure 7.** Minimum, average and maximum isopleths of Zr-in-rutile from LR04 (a), LR05 (a), LR10C (b) and LR44C (c) samples. And minimum, average and maximum isopleths of Ti-in-quartz for LR44C sample (c). Peak assemblage pseudosection fields are those of Fig. 3. Isopleths of Zr-in-rutile were calculated using the calibration of Tomkins *et al.* (2007) and Ti-in-quartz using the calibration of Thomas *et al.* (2010). Yellow star in c indicates the intersection of maximum values of Ti-in-quartz and Zr-in-rutile.

are presented based on pre-peak, peak and post-peak mineral assemblages (Fig. 11).

Peak mineral assemblages indicate that the metamorphic grade increases from high pressure lower amphibolite facies conditions in the north (Chl + Ky + St + Rt) to high pressure

amphibolite facies in the central portion (St + Bt + Grt + Rt), and to eclogite facies in the southern portion (St + Ky + Grt + Rt). The high-pressure Al-silicate, kyanite, is stable in the studied rocks, consistent with the metamorphic high-pressure conditions which the samples were submitted. Due to the lack

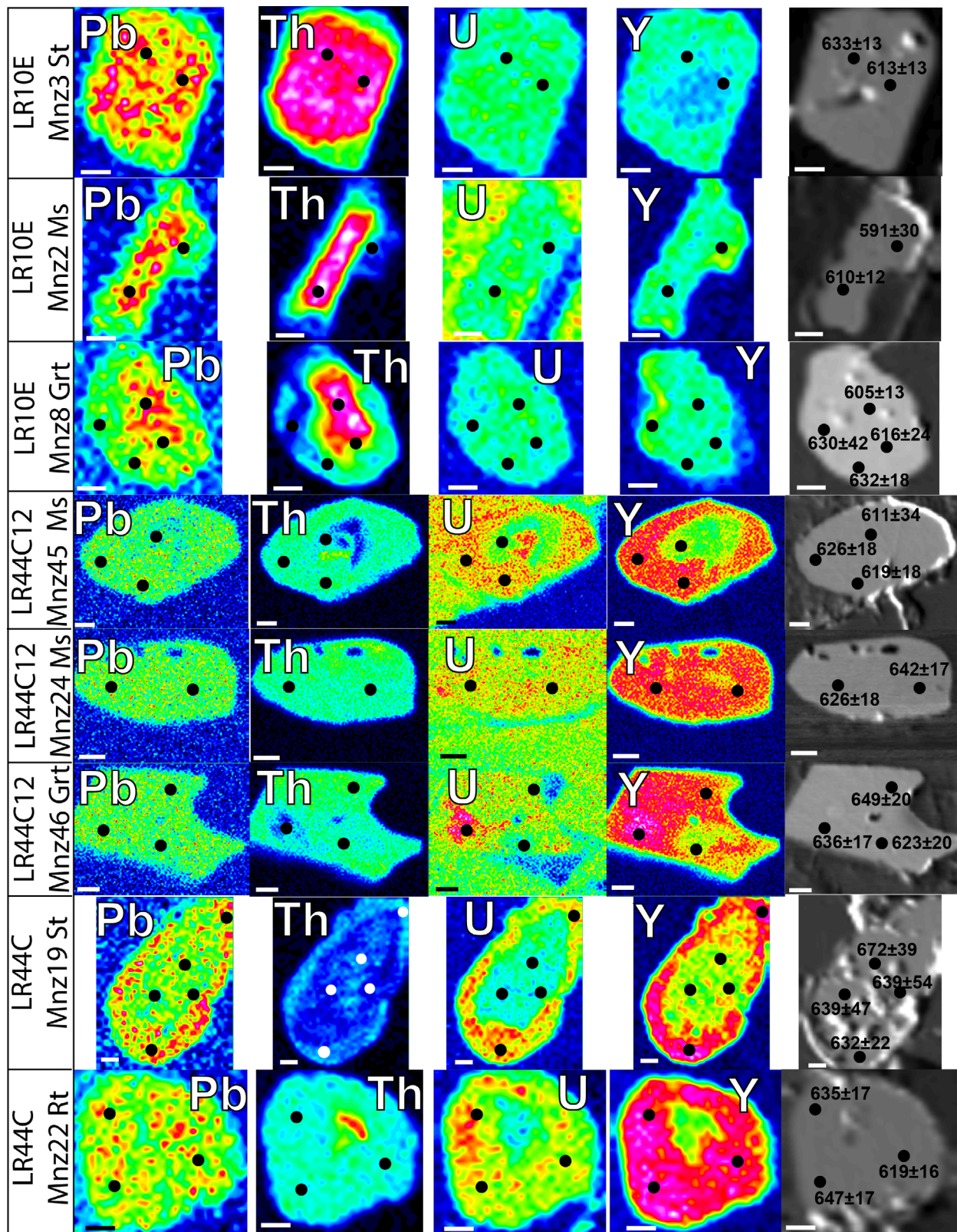


**Figure 8.** Representative compositional X-ray maps and back-scattered electron (BSE) images of analyzed monazite showing the compositional variance in different crystals. Circles (white or black) indicate the analyses localization. Annotations on the left hand side of the image indicate the sample, the monazite identification (as in Tab. 4) and the textural context of the crystal (e.g., LR10E Mnz23 St: monazite number 23, from LR10E sample, that is included in staurolite). Age is presented in Ma. Scale bars in all images measure 5 microns.

Table S. Electron microprobe analysis (EPMA) of monazite major and trace element composition. Values are in element %wt. Detection limits are those presented in Table 1.

Sample	Spot #	Texture	Y	Si	Al	Th	Ca	La	Ce	Pr	Nd	Sm	Fe	Gd	Er	Tb	Dy	Yb	U	S	P	Pb
LR10E	Mnz12_1	Incl Grt	0.87	0.12	0.45	2.14	0.40	9.81	20.91	2.08	9.46	1.28	7.31	0.85	BD	BD	0.39	BD	0.22	0.03	11.06	0.09
LR10E	Mnz12_2	Incl Grt	0.42	0.12	0.11	2.43	0.46	11.34	23.46	2.42	10.24	1.50	1.38	0.97	BD	BD	BD	BD	0.29	BD	11.40	0.10
LR10E	Mnz4_1	Mtx	0.54	0.25	BD	7.87	1.11	9.37	20.07	2.08	9.60	1.50	0.20	1.40	BD	BD	0.38	BD	0.47	BD	12.04	0.27
LR10E	Mnz4_2	Mtx	0.80	0.36	0.31	3.44	0.57	10.52	22.24	2.26	10.04	1.60	0.27	1.35	BD	BD	0.44	BD	0.34	BD	12.24	0.13
LR10E	Mnz4_3	Mtx	0.16	2.85	3.17	3.06	0.45	10.20	20.72	1.98	9.89	1.68	0.42	1.07	BD	BD	BD	BD	0.32	BD	11.41	0.11
LR10E	Mnz3_1	Incl St	0.20	0.29	0.01	8.77	1.26	9.71	20.13	2.16	9.33	1.54	0.49	1.03	BD	BD	BD	BD	0.47	BD	11.84	0.29
LR10E	Mnz3_2	Incl St	0.41	0.30	0.01	8.74	1.16	9.27	20.26	2.06	9.58	1.56	0.48	1.52	BD	BD	0.30	BD	0.46	BD	11.90	0.30
LR10E	Mnz2_1	Mtx	0.40	0.37	0.01	9.65	1.25	9.17	18.95	1.96	9.08	1.70	0.46	1.48	BD	BD	0.29	BD	0.49	BD	11.96	0.32
LR10E	Mnz2_2	Mtx	0.59	0.08	0.01	2.62	0.40	11.29	22.87	2.30	10.78	1.60	0.38	1.43	BD	BD	0.43	BD	0.32	BD	12.40	0.11
LR10E	Mnz1_1	Mtx	0.43	0.38	BD	9.84	1.26	8.95	19.03	1.96	9.08	1.58	0.08	1.55	BD	BD	BD	BD	0.49	BD	11.68	0.32
LR10E	Mnz1_2	Mtx	0.46	0.29	BD	8.18	1.14	9.39	20.40	1.93	9.48	1.58	0.13	1.59	BD	0.23	0.31	BD	0.45	BD	11.90	0.27
LR10E	Mnz1_4	Mtx	0.12	0.13	0.05	2.70	0.45	11.01	23.07	2.50	10.84	1.92	0.14	1.32	BD	BD	BD	BD	0.31	BD	12.18	0.10
LR10E	Mnz8_1	Incl Grt	0.46	0.28	0.01	8.49	1.23	9.43	19.73	1.94	9.48	1.53	0.88	1.42	BD	0.22	0.22	BD	0.46	0.02	11.98	0.28
LR10E	Mnz8_2	Incl Grt	0.05	0.71	0.45	3.74	0.73	10.48	21.88	2.37	10.15	1.75	1.96	1.04	BD	BD	BD	BD	0.42	BD	11.90	0.14
LR10E	Mnz8_3	Incl Grt	0.49	0.14	0.01	5.37	0.86	10.42	21.28	2.36	10.08	1.64	0.86	1.41	BD	BD	0.29	BD	0.38	BD	12.23	0.20
LR10E	Mnz8_4	Incl Grt	0.47	0.15	0.08	1.82	0.34	11.70	23.10	2.30	10.40	1.62	1.31	1.20	BD	BD	0.37	BD	0.25	BD	12.34	0.08
LR10E	Mnz7_1	Incl Grt	0.42	0.34	BD	9.77	1.37	9.05	19.06	1.94	9.27	1.56	0.86	1.47	BD	BD	0.30	BD	0.49	BD	11.88	0.33
LR10E	Mnz7_2	Incl Grt	0.67	0.12	0.03	2.55	0.44	11.12	22.24	2.35	10.47	1.75	1.27	1.47	BD	BD	0.34	BD	0.28	BD	12.23	0.10
LR10E	Mnz7_3	Incl Grt	0.17	0.66	0.46	2.78	0.48	10.93	22.67	2.28	10.17	1.69	1.90	1.15	BD	BD	BD	BD	0.28	BD	12.01	0.11
LR10E	Mnz9_1	Mtx	0.33	0.10	BD	4.10	0.60	10.15	21.84	2.08	10.56	1.86	0.12	1.50	BD	BD	BD	BD	0.33	BD	12.19	0.15
LR10E	Mnz9_2	Mtx	0.50	0.05	0.01	1.68	0.28	10.99	22.79	2.22	11.20	1.90	0.26	1.65	BD	BD	0.27	BD	0.22	BD	12.34	0.07
LR10E	Mn15_1	Incl Grt	0.38	0.11	BD	4.15	0.66	10.40	21.62	2.56	10.15	1.70	0.24	1.76	BD	BD	0.32	BD	0.34	BD	12.27	0.15
LR10E	Mn15_2	Incl Grt	0.40	0.13	BD	4.88	0.74	9.89	21.48	2.36	9.63	2.07	0.31	1.95	BD	BD	0.30	BD	0.41	BD	12.20	0.18
LR10E	Mn15_3	Incl Grt	0.26	0.18	BD	6.07	0.90	10.43	21.07	2.29	9.91	1.52	0.97	1.36	BD	BD	0.21	BD	0.42	BD	12.11	0.21
LR10E	Mn15_4	Incl Grt	0.25	0.15	BD	5.32	0.84	10.57	21.34	2.47	10.31	1.64	0.52	1.28	BD	BD	BD	BD	0.39	BD	12.14	0.18
LR10E	Mn15_5	Incl Grt	0.34	0.17	0.03	4.39	0.72	10.33	21.78	2.10	10.09	1.74	0.89	1.71	BD	0.24	0.33	BD	0.39	BD	12.18	0.16
LR44C	Mnz19_1	Incl St	0.83	0.05	0.02	1.46	0.25	12.03	24.42	2.28	9.41	1.38	0.24	0.99	BD	BD	0.34	BD	0.22	BD	12.29	0.07
LR44C	Mnz19_2	Incl St	0.96	0.10	0.05	1.50	0.32	11.30	25.01	2.30	9.91	1.36	0.28	1.12	BD	0.13	0.36	BD	0.35	BD	12.38	0.09
LR44C	Mnz19_3	Incl St	0.81	0.13	0.10	1.16	0.21	11.81	25.60	2.36	9.69	1.60	0.29	1.17	BD	BD	0.39	BD	0.21	BD	12.28	0.06
LR44C	Mnz19_4	Incl St	1.45	0.02	0.02	1.62	0.48	10.71	23.81	2.14	9.26	1.41	0.42	1.37	BD	0.28	0.54	BD	1.05	BD	12.33	0.16
LR44C	Mnz1_1	Incl St	1.45	0.01	BD	3.80	0.74	10.25	22.34	2.25	8.79	1.48	0.24	1.21	BD	BD	0.44	BD	0.93	BD	12.46	0.21
LR44C	Mnz22_1	Incl Rt	1.36	0.03	0.01	3.91	0.75	9.49	22.58	2.20	9.35	1.46	0.35	1.01	BD	0.12	0.52	BD	0.95	BD	12.38	0.21
LR44C	Mnz22_2	Incl Rt	1.49	0.01	BD	3.37	0.72	9.91	21.99	2.05	8.84	1.49	0.30	1.23	BD	BD	0.45	BD	0.96	BD	12.37	0.21
LR44C	Mnz22_3	Incl Rt	1.51	0.01	BD	3.21	0.75	10.07	22.74	1.99	8.72	1.27	0.43	1.17	BD	BD	0.54	BD	1.09	BD	12.45	0.21
LR44C	Mnz23_1	Mtx	1.58	0.03	0.02	3.42	0.80	9.98	22.16	2.11	9.00	1.54	0.08	1.30	BD	0.29	0.52	BD	1.11	BD	12.58	0.22
LR44C	Mnz23_2	Mtx	1.28	0.12	0.07	3.25	0.64	10.40	23.12	2.29	9.17	1.42	0.12	1.10	BD	BD	0.37	BD	0.75	BD	12.36	0.17
LR44C	Mnz23_3	Mtx	1.48	0.02	0.01	3.44	0.76	9.97	22.48	2.06	9.29	1.33	0.10	1.16	BD	BD	0.46	BD	0.97	BD	12.43	0.21

Continue...

Table 5. Continuation.

Sample	Spot #	Texture	Y	Si	Al	Th	Ca	La	Ce	Pr	Nd	Sm	Fe	Gd	Er	Tb	Dy	Yb	U	S	P	Pb
LR44C	Mnz26_3	Mtx	1.36	0.03	0.01	3.35	0.72	10.03	23.26	2.15	9.15	1.39	0.05	1.15	BD	BD	0.45	BD	1.02	BD	12.42	0.20
LR44C	Mnz20_1	Mtx	1.27	0.02	BD	3.98	0.75	9.92	22.17	2.05	9.68	1.59	0.10	1.13	BD	BD	0.46	BD	0.74	BD	12.46	0.20
LR44C	Mnz20_2	Mtx	1.43	0.01	0.01	3.39	0.74	10.42	22.62	2.12	9.04	1.31	0.11	1.08	0.14	BD	0.40	BD	0.95	BD	12.41	0.21
LR44C	Mnz21_2	Mtx	1.54	0.01	BD	3.82	0.85	9.90	21.99	2.07	9.22	1.46	0.05	1.25	0.11	BD	0.47	BD	1.16	BD	12.36	0.24
LR44C	Mnz24_1	Mtx	1.44	0.02	0.01	3.53	0.77	10.13	22.29	2.15	9.26	1.47	BD	1.06	BD	BD	0.45	BD	0.93	BD	12.43	0.20
LR44C	Mnz24_2	Mtx	1.47	0.03	0.01	3.54	0.78	10.08	22.01	2.11	9.51	1.26	BD	1.04	0.12	0.25	0.44	BD	0.95	BD	12.47	0.21
LR44C	Mnz22_1	Mtx	1.47	0.03	BD	3.54	0.71	10.12	22.65	2.16	9.25	1.38	0.24	1.26	BD	BD	0.49	BD	0.94	BD	12.49	0.20
LR44C	Mnz22_2	Mtx	0.71	0.06	0.04	2.84	0.54	8.53	18.68	1.78	7.65	1.18	0.08	0.77	BD	BD	0.33	BD	0.40	BD	10.98	0.13
LR44C	Mnz22_3	Mtx	1.44	0.01	BD	3.37	0.68	10.10	22.83	2.17	9.01	1.51	0.10	1.15	BD	BD	0.56	BD	0.94	BD	12.55	0.20
LR44C	Mnz5_1	Incl Grt	0.85	0.12	0.01	5.92	0.99	9.01	21.39	2.33	10.23	1.46	0.81	1.16	BD	BD	0.36	BD	0.40	BD	12.28	0.21
LR44C	Mnz4_1	Incl Grt	0.92	0.04	0.01	2.90	0.57	10.22	22.21	1.98	9.10	1.30	1.32	0.82	BD	BD	0.41	BD	0.47	BD	11.76	0.14
LR44C	Mnz4_2	Incl Grt	0.56	7.09	4.76	1.75	0.46	6.22	14.57	1.27	5.94	0.82	12.18	0.61	BD	BD	0.31	BD	0.36	BD	7.88	0.09
LR44C	Mnz45_1	Mtx	0.80	0.03	0.01	1.76	0.37	12.44	25.74	2.28	8.82	1.12	0.33	0.73	BD	BD	0.28	BD	0.43	BD	12.45	0.10
LR44C	Mnz45_2	Mtx	1.25	0.02	0.01	3.32	0.71	9.66	22.06	2.09	8.96	1.40	0.22	1.09	BD	BD	0.47	BD	0.89	BD	11.96	0.19
LR44C	Mnz45_3	Mtx	1.45	0.02	0.01	3.54	0.78	9.67	22.54	2.22	9.73	1.53	0.22	1.15	BD	BD	0.52	BD	0.93	BD	12.44	0.20
LR44C	Mnz11_1	Mtx	1.53	0.04	0.03	3.25	0.69	10.27	22.69	2.20	9.46	1.43	BD	1.17	BD	BD	0.47	BD	1.05	BD	12.46	0.21
LR44C	Mnz11_2	Mtx	1.20	0.07	0.02	3.16	0.62	10.72	23.36	2.20	9.56	1.34	BD	1.32	BD	BD	0.37	BD	0.67	BD	12.41	0.16
LR44C	Mnz46_1	Incl Grt	1.63	0.02	BD	2.60	0.66	10.04	22.48	2.17	9.67	1.45	0.05	1.25	BD	BD	0.49	BD	1.22	BD	12.44	0.21
LR44C	Mnz46_2	Incl Grt	1.42	0.03	0.01	3.58	0.78	10.02	22.05	1.98	9.02	1.56	0.07	1.22	BD	BD	0.54	BD	0.99	BD	12.40	0.22
LR44C	Mnz46_3	Incl Grt	0.99	0.04	0.01	3.32	0.67	10.82	22.89	2.16	9.42	1.37	BD	1.03	BD	BD	0.40	BD	0.73	BD	12.39	0.17
LR44C	Mnz32_1	Mtx	1.42	0.03	0.01	3.61	0.78	10.18	22.49	2.12	8.98	1.30	0.18	1.21	BD	BD	0.45	BD	0.94	BD	12.37	0.20
LR44C	Mnz32_2	Mtx	0.67	0.04	0.01	4.08	0.67	6.91	23.61	2.57	12.41	1.72	0.17	0.88	BD	BD	0.37	BD	0.40	BD	12.37	0.16
LR44C	Mnz33_1	Incl Ky	1.37	0.02	0.02	3.56	0.72	10.21	22.05	2.11	8.77	1.39	0.09	0.97	BD	0.24	0.54	BD	0.89	BD	12.57	0.20
LR44C	Mnz42_1	Mtx	1.40	0.01	0.01	3.45	0.72	10.14	22.26	2.35	9.78	1.61	0.20	1.25	BD	BD	0.59	BD	0.88	BD	12.53	0.20
LR44C	Mnz42_2	Mtx	1.39	0.01	0.01	3.84	0.78	10.19	22.54	2.04	9.31	1.50	0.19	1.22	BD	BD	0.44	BD	0.85	BD	12.49	0.20
LR44C	Mnz44_1	Mtx	1.42	0.01	BD	3.33	0.74	10.80	22.85	2.24	9.11	1.42	0.06	1.08	BD	BD	0.50	BD	0.96	BD	12.45	0.19
LR44C	Mnz44_2	Mtx	1.55	0.02	0.01	3.47	0.75	9.98	22.35	2.24	9.32	1.46	BD	1.44	0.15	BD	0.48	0.16	1.03	BD	12.45	0.21
LR44C	Mnz47_1	Mtx	1.23	0.10	0.01	3.82	0.65	10.43	22.97	2.11	8.91	1.45	0.11	1.08	BD	BD	0.39	BD	0.60	BD	12.31	0.18
LR44C	Mnz47_2	Mtx	1.30	0.12	0.02	3.76	0.69	10.34	22.83	2.04	9.18	1.35	0.25	1.21	BD	BD	0.55	BD	0.69	BD	12.24	0.18
LR44C	Mnz48_1	Mtx	1.34	0.01	BD	3.28	0.64	10.34	22.72	2.16	9.45	1.43	0.13	1.25	BD	BD	0.41	BD	0.86	BD	12.45	0.19
LR44C	Mnz48_2	Mtx	1.55	0.02	0.01	3.72	0.78	9.88	22.23	2.19	9.19	1.41	0.10	1.33	BD	BD	0.52	BD	0.97	BD	12.41	0.22
LR44C	Mnz49_1	Mtx	1.48	0.03	0.01	3.53	0.75	10.04	22.50	2.17	9.05	1.37	0.11	1.31	BD	BD	0.56	BD	0.95	BD	12.48	0.21
LR44C	Mnz49_3	Mtx	1.47	0.02	0.01	3.88	0.83	9.97	22.16	2.25	8.77	1.56	0.15	1.23	BD	BD	0.46	BD	0.94	BD	12.50	0.22
LR44C	Mnz49_4	Mtx	1.47	0.01	0.01	3.28	0.72	9.93	22.91	2.22	9.18	1.57	0.16	1.30	BD	BD	0.33	BD	0.96	BD	12.47	0.20
LR44C	Mnz29_1	Incl St	0.76	0.07	0.01	4.03	0.68	9.24	23.54	2.27	10.89	1.48	0.43	0.99	BD	BD	BD	BD	0.45	BD	12.23	0.17
LR44C	Mnz29_2	Incl St	1.31	0.04	0.01	3.23	0.67	10.51	22.81	2.13	9.29	1.36	0.52	1.10	BD	BD	0.50	BD	0.88	BD	12.46	0.19

BD: below the detection limit.

of plagioclase, quantification of pressure conditions is problematic. Even when mineral composition isopleths are calculated and presented in the respective fields of the pseudosections, they form sub-parallel lines, and their crossing results in large uncertainties when pressure is calculated.

Post-tectonic chloritoid (to  $S_{1/2}$ ) in LR04 sample (Fig. 2B) is interpreted as a retrograde phase in respect to peak condition attained under high pressure lower amphibolite facies (northern portion). In the high pressure amphibolite facies rocks from the central portion (Fig. 2D), chlorite overgrows the main foliation and is interpreted as retrograde. Chloritoid porphyroblasts associated with staurolite are present in a specific compositional layer in LR10E sample (Fig. 2F). Two possible

interpretations for this association are presented here. The first hypothesis is that chloritoid occurrence is controlled by the chemical composition of the layer. Another one is that the chloritoid is pre-tectonic and was preserved only in this band. Since staurolite has a subhedral shape, we interpret that staurolite is replacing chloritoid. We acknowledge that the metamorphic texture is complex and an opposite interpretation, in which chloritoid replaces staurolite, cannot be ruled out.

The metamorphic peak assemblage observed in samples from the southern portion of Luminárias Nappe is represented by  $St + Ky + Grt + Rt$ , which indicate the highest temperature and pressure condition observed in the region. According to the calculated pseudosection, this metamorphic peak assemblage

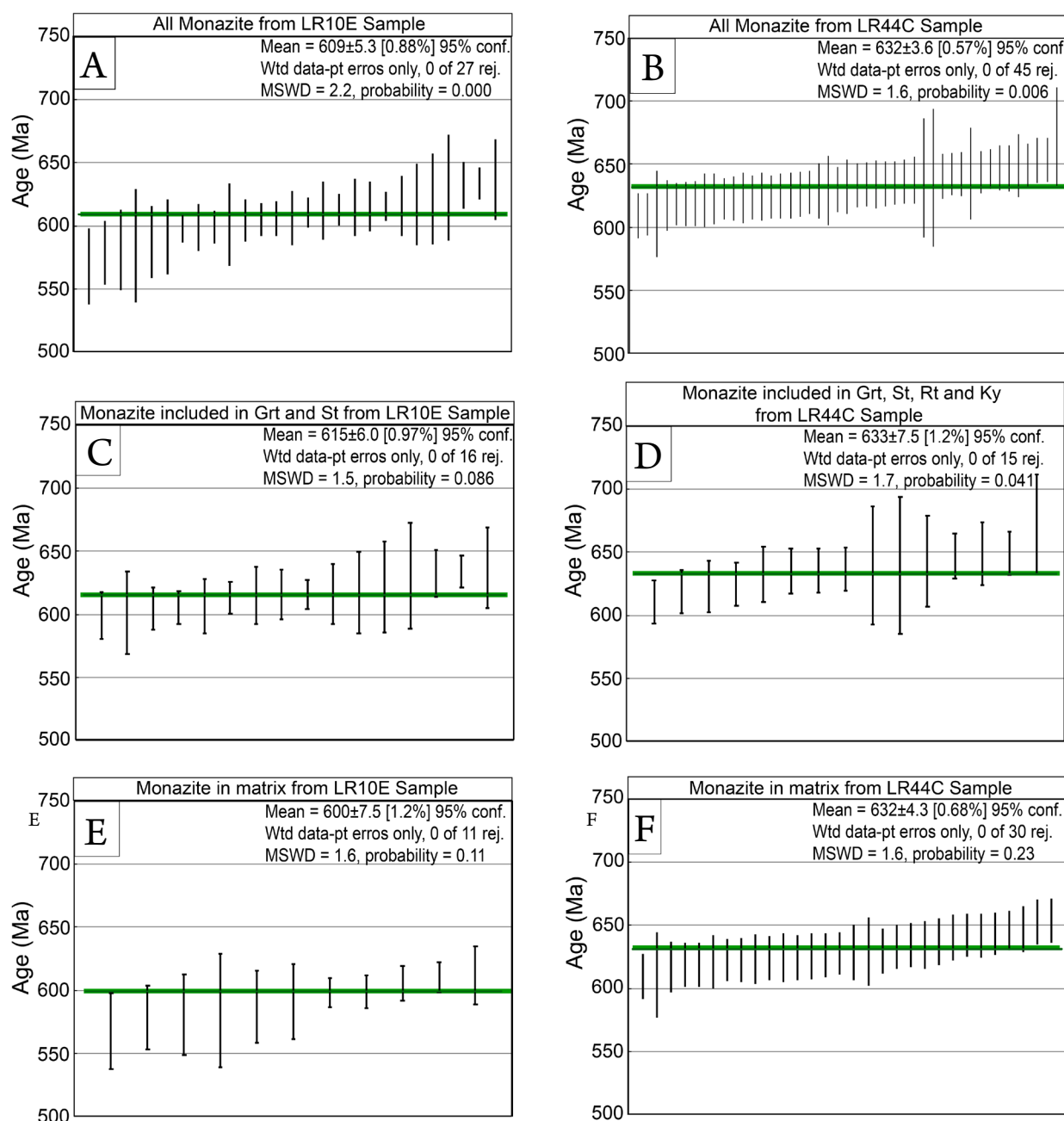


**Figure 9.** Error-weighted average of U–Th–Pb<sub>T</sub> EPMA ages of monazite. (A) Data from all analyzed monazite from LR10E sample. (B) Data from all analyzed monazite from LR44C sample. (C) Data from included monazite in garnet and staurolite from LR10E sample. (D) Data from included monazite in garnet, staurolite, kyanite and rutile from LR44C sample. (E) Data from monazite in the matrix from LR10E sample. (F) Data from monazite in the matrix from LR44C sample. Green lines show the mean values. Data-point error symbols are all 2 sigma. Wtd: weighted, conf.: confidence, rej.: rejected and MSWD: Mean Square of Weighted Derivates.

**Table 6.** Corrected concentrations of Th, U and Pb (in ppm) and calculated ages (Ma) for the analyzed monazite.

Sample	Spot #	Texture	Th		U		Pb		Age	
			Meas	2Sig	Meas	2Sig	Meas	2Sig	Calc	2Sig
LR10E	Mnz12_1	Incl Grt	21,419	221	2,080	68	791	48	621	36
LR10E	Mnz12_2	Incl Grt	24,260	233	2,776	72	903	51	601	32
LR10E	Mnz5_2	Mtx	19,522	217	4,292	78	984	50	648	31
LR10E	Mnz4_1	Mtx	78,653	378	4,315	74	2,533	60	606	14
LR10E	Mnz4_2	Mtx	34,412	265	3,242	74	1,173	53	578	25
LR10E	Mnz4_3	Mtx	30,645	254	3,041	73	1,074	55	587	29
LR10E	Mnz3_1	Incl St	87,724	395	4,288	73	2,811	60	613	13
LR10E	Mnz3_2	Incl St	87,416	393	4,164	73	2,886	60	633	13
LR10E	Mnz2_1	Mtx	96,547	415	4,490	75	3,060	62	610	12
LR10E	Mnz2_2	Mtx	26,234	239	3,117	75	970	51	591	30
LR10E	Mnz1_1	Mtx	98,405	413	4,427	74	3,042	61	598	11
LR10E	Mnz1_2	Mtx	81,755	384	4,099	73	2,569	59	599	13
LR10E	Mnz1_4	Mtx	26,962	240	2,921	73	956	55	581	32
LR10E	Mnz8_1	Incl Grt	84,877	390	4,181	74	2,687	60	605	13
LR10E	Mnz8_2	Incl Grt	37,423	273	3,984	76	1,401	57	616	24
LR10E	Mnz8_3	Incl Grt	53,717	317	3,587	74	1,866	57	632	18
LR10E	Mnz8_4	Incl Grt	18,193	209	2,381	73	740	52	630	42
LR10E	Mnz7_1	Incl Grt	97,720	410	4,472	74	3,116	61	615	12
LR10E	Mnz7_2	Incl Grt	25,452	237	2,681	73	952	52	617	32
LR10E	Mnz7_3	Incl Grt	27,750	244	2,681	72	1,050	54	637	32
LR10E	Mnz9_1	Mtx	41,032	283	3,152	73	1,416	56	612	23
LR10E	Mnz9_2	Mtx	16,834	204	2,151	72	628	50	584	45
LR10E	Mn15_1	Incl Grt	41,474	286	3,195	73	1,439	56	615	23
LR10E	Mn15_2	Incl Grt	48,773	307	3,902	75	1,707	57	615	20
LR10E	Mn15_3	Incl Grt	60,663	334	3,879	74	1,998	58	604	17
LR10E	Mn15_4	Incl Grt	53,184	319	3,634	74	1,755	57	599	19
LR10E	Mn15_5	Incl Grt	43,940	294	3,653	75	1,528	56	606	21
LR44C	Mnz19_1	Incl St	14,615	196	2,111	72	622	48	639	47
LR44C	Mnz19_2	Incl St	15,034	197	3,407	76	797	49	672	39
LR44C	Mnz19_3	Incl St	11,589	182	1,999	72	524	47	640	55
LR44C	Mnz19_4	Incl St	16,230	201	10,422	93	1,442	53	632	22
LR44C	Mnz1_1	Incl St	38,008	277	9,148	90	1,918	56	625	17
LR44C	Mnz1_2	Incl St	35,157	267	3,207	73	1,211	52	589	24
LR44C	Mnz22_1	Incl Rt	39,057	277	9,263	90	1,939	56	619	17
LR44C	Mnz22_2	Incl Rt	33,689	263	9,439	91	1,892	55	647	18
LR44C	Mnz22_3	Incl Rt	32,089	257	10,719	93	1,931	56	635	17
LR44C	Mnz23_1	Mtx	34,189	263	10,974	94	1,974	56	623	17
LR44C	Mnz23_2	Mtx	32,531	260	7,323	86	1,575	54	617	20
LR44C	Mnz23_3	Mtx	34,437	265	9,530	91	1,880	55	634	17
LR44C	Mnz26_1	Mtx	32,763	259	12,550	84	1,818	55	547	16
LR44C	Mnz26_2	Mtx	36,655	271	12,487	84	1,852	55	532	15
LR44C	Mnz26_3	Mtx	33,546	262	10,000	92	1,870	56	624	17
LR44C	Mnz20_1	Mtx	39,788	282	7,198	85	1,825	56	637	18
LR44C	Mnz20_2	Mtx	33,872	264	9,368	90	1,909	56	653	18
LR44C	Mnz21_2	Mtx	38,201	275	11,398	95	2,210	57	646	16
LR44C	Mnz24_1	Mtx	35,328	268	9,101	89	1,844	55	626	18
LR44C	Mnz24_2	Mtx	35,416	269	9,334	91	1,917	55	642	17

Continue...

Table 6. Continuation.

Sample	Spot #	Texture	Th		U		Pb		Age	
			Meas	2Sig	Meas	2Sig	Meas	2Sig	Calc	2Sig
LR44C	Mnz22_1	Mtx	35,380	269	9,238	91	1,835	55	619	18
LR44C	Mnz22_2	Mtx	28,392	244	3,816	74	1,162	53	630	27
LR44C	Mnz22_3	Mtx	33,700	263	9,260	91	1,855	55	641	18
LR44C	Mnz5_1	Incl Grt	59,198	332	3,761	74	1,968	57	611	17
LR44C	Mnz5_2	Incl Grt	57,832	330	4,241	73	2,207	58	681	17
LR44C	Mnz4_1	Incl Grt	28,975	246	4,599	77	1,292	52	649	25
LR44C	Mnz4_2	Incl Grt	17,543	207	3,479	73	841	50	643	36
LR44C	Mnz45_1	Mtx	17,583	207	4,191	78	863	51	611	34
LR44C	Mnz45_2	Mtx	33,203	262	8,758	88	1,749	54	626	18
LR44C	Mnz45_3	Mtx	35,378	269	9,110	89	1,823	55	619	18
LR44C	Mnz11_1	Mtx	32,545	260	10,310	93	1,903	55	634	17
LR44C	Mnz11_2	Mtx	31,633	256	6,577	84	1,492	54	622	21
LR44C	Mnz46_1	Incl Grt	25,968	239	12,122	97	1,892	55	636	17
LR44C	Mnz46_2	Incl Grt	35,790	268	9,750	91	1,990	56	649	17
LR44C	Mnz46_3	Incl Grt	33,239	259	7,182	85	1,596	55	623	20
LR44C	Mnz32_1	Mtx	36,118	271	9,185	90	1,863	55	623	17
LR44C	Mnz32_2	Mtx	40,843	286	3,781	75	1,510	55	629	22
LR44C	Mnz33_1	Incl Ky	35,621	271	8,734	89	1,843	55	635	18
LR44C	Mnz42_1	Mtx	34,492	266	8,602	89	1,835	55	647	18
LR44C	Mnz42_2	Mtx	38,443	277	8,351	88	1,873	56	630	18
LR44C	Mnz44_1	Mtx	33,267	259	9,438	91	1,766	55	610	18
LR44C	Mnz44_2	Mtx	34,651	267	10,091	92	1,922	55	628	17
LR44C	Mnz47_1	Mtx	38,211	275	5,830	81	1,613	54	623	20
LR44C	Mnz47_2	Mtx	37,648	275	6,754	84	1,686	54	625	19
LR44C	Mnz48_1	Mtx	32,789	259	8,399	88	1,730	55	635	19
LR44C	Mnz48_2	Mtx	37,191	271	9,475	91	1,982	55	642	17
LR44C	Mn49_1	Mtx	35,292	268	9,373	90	1,953	55	654	17
LR44C	Mn49_2	Mtx	37,360	273	9,221	89	2,034	56	665	17
LR44C	Mn49_3	Mtx	38,760	279	9,164	90	2,002	56	644	17
LR44C	Mn49_4	Mtx	32,823	259	9,481	90	1,803	55	625	18
LR44C	Mnz29_1	Incl St	40,323	282	4,339	77	1,597	55	648	21
LR44C	Mnz29_2	Incl St	32,339	259	8,651	89	1,736	55	633	19

Meas: measured, 2Sig: 2 sigma error. Calc: calculated ages.

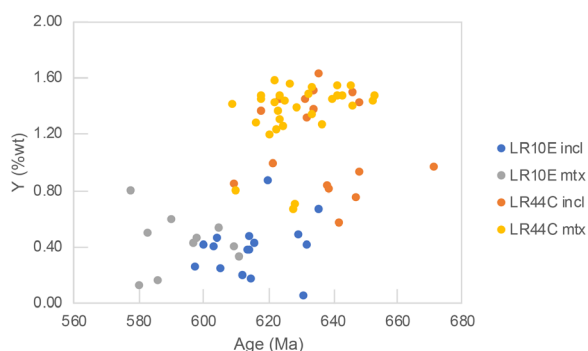


Figure 10. Y (%wt) content variation among monazite textural varieties and between samples versus the age (Ma). Incl: included crystals. Mtx: crystals in the matrix.

is formed under eclogite facies conditions (Fig. 11). Staurolite occurs as inclusions in garnet porphyroblasts. Kyanite also occurs as inclusions in garnet, but only in the rim. Both staurolite and kyanite happen as oriented crystals in the matrix defining the foliation (Fig. 2G). Biotite and chlorite with no preferred orientation are observed in several samples from the southern portion and are interpreted as retrorade phases.

Taking into consideration mineral assemblages, the textural relationships and the stability fields obtained in the pseudo-section, clock-wise  $P$ - $T$  paths can be defined for the studied samples (Fig. 11). No pseudo-section has been calculated for northern portion samples (LR04 and LR05). Peak  $T$  condition ( $580 \pm 4^\circ\text{C}$  at *ca.* 0.9 GPa) is given by the Zr content

in rutile from LR04 sample and is compatible with the peak mineral assemblage Chl + Ky + St + Rt. The post-peak path is characterized by the crystallization of post-tectonic chloritoid (Fig. 2B). For the central portion (LR10C and LR10E samples), the  $P$ - $T$  path starts in the stability field of the Chl + Cld + Grt + Rt assemblage (Fig. 11B). The replacement of chloritoid by staurolite (Fig. 2F) and the biotite presence (Fig. 2D) indicate that the  $P$ - $T$  path crosses the Chl + St + Grt + Rt field, reaching the Bt + St + Grt + Rt field in peak metamorphic conditions. Post-peak metamorphism is evidenced by chlorite and ilmenite crystallization (Fig. 2E) in the Chl + St + Grt + Ilm field (Fig. 11B). For the southern portion (LR44C sample), the  $P$ - $T$  path starts in the stability field of the St + Grt + Rt assemblage, reaches the metamorphic peak at the St + Ky + Grt + Rt assemblage field, crossing through Bt + St + Grt + Rt and Bt + St + Grt + Ilm fields, finishing in the retrograde assemblage Chl + St + Grt + Ilm field (Figs. 4B and 10C).

Metamorphism temperature in the Luminárias Nappe rocks is close to the temperature of resetting of Zr in rutile, at *ca.* of 550–650°C (Cherniak 2000, Cherniak *et al.* 2007, Treibold *et al.* 2007, Triebold *et al.* 2012, Kooijam *et al.* 2010, Kohn *et al.* 2016, Cruz-Uribe *et al.* 20018). Although the Zr content in rutile from LR04 sample provides consistent results, the registered temperature is lower than the expected re-equilibration rutile temperature. It is noteworthy that the temperature of *ca.* 580°C obtained for this sample agrees with the peak mineral assemblage (KFMASH petrogenic grid in White *et al.* 2014). According to Cruz-Uribe *et al.* (2018), single element thermometers in temperatures lower than 600°C can only be applied if trace element equilibrium can be demonstrated. This is the case of the studied samples, in which quartz, rutile and zircon are present, buffering the equilibrium of the  $\text{SiO}_2$  -  $\text{TiO}_2$  -  $\text{ZrO}_2$  system.

In LR44C sample, only rutile crystals included in garnet have Zr content above the EPMA detection limit, indicating that post-peak metamorphism may have changed the rutile composition in the matrix. Higher content of Zr in rutile is often observed in crystals included in garnet and kyanite (Zack *et al.* 2004, Luvizotto *et al.* 2009, Hart *et al.* 2018).

With the trace element data, a correlation between Nb content in rutile and the occurrence of biotite is interpreted. Higher Nb content in rutile is correlated with the absence of biotite (rutile in LR04 and LR05 samples and rutile included in garnet in LR44C sample, where peak assemblage is biotite free). As pointed out before by Luvizotto & Zack (2009), high Nb content in rutile can be linked to rutile growth associated with biotite breakdown during prograde metamorphism, since rutile favors Nb over Ti, when compared to biotite. In LR10C and LR10E samples, rutile with lower Nb content occurs in the matrix where rutile coexists with biotite in the peak metamorphic assemblage. In LR44C sample, biotite is retro-metamorphic and only occurs in the matrix where the rutile also presents lower Nb content. According to our data (Fig. 4B), biotite retro-metamorphic crystallization in the presence of rutile in LR44C sample occurs in  $T$  conditions between 590°C (lowest  $T$  stability in Fig. 4B) and 630°C (peak  $T$  condition) and  $P$  conditions lower than 1.05 GPa (highest  $P$  stability in Fig. 4B).

Pressure conditions of the metamorphic peak are higher than the Barrovian metamorphism. High-pressure conditions were also obtained by Silva (2010) in the Carrancas Klippe, northeast of the Luminárias Nappe. The author calculated peak  $P$ - $T$  conditions ( $1.0 \pm 0.17$  GPa and  $577 \pm 8^\circ\text{C}$  in the north and  $1.29 \pm 0.1$  GPa and  $608.5 \pm 19.5^\circ\text{C}$  in the south), which are similar to those presented here, and somewhat higher in pressure than previously calculated for these units (Campos Neto & Caby 1999).

The basal unit gneiss from the São Vicente Complex and/or A1/A2 (Fig. 1) has plagioclase. Lenses of amphibolite are common in this unit. Mineral assemblages in both rocks are incompatible with eclogite facies metamorphic conditions. It may suggest that either the high-pressure conditions calculated here are overestimated or that the Carrancas Group was thrust over the São Vicente Complex after metamorphic peak conditions, and that they are, therefore, unrelated as suggested by recent data (Westin *et al.* 2016, 2019).

## Age of metamorphism

Three distinct U-Th-Pb<sub>T</sub> monazite ages (Fig. 9) have been obtained for the Luminárias Nappe rocks:  $600 \pm 8$  Ma for matrix

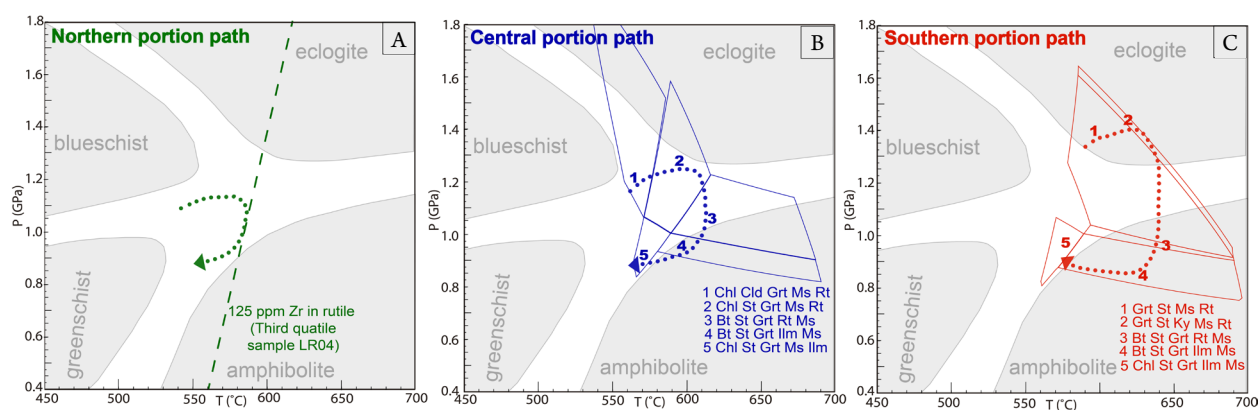


**Figure 11.** Pressure-temperature-time ( $P$ - $T$ - $t$ ) paths for the three portions of metapelites from the Luminárias Nappe based on textural relationships, pseudosection modelling, Zr-in-rutile and Ti-in-quartz and geochronology EPMA geochronology of monazite. (A) ( $P$ - $T$ - $t$ ) path from the northern portion. (B) ( $P$ - $T$ - $t$ ) path from the central portion (pseudosections fields from fig. 4a with quartz and  $\text{H}_2\text{O}$  in excess). (C) ( $P$ - $T$ - $t$ ) path from the southern portion (pseudosections fields from fig. 4B with quartz and  $\text{H}_2\text{O}$  in excess). Pressure-temperature fields of metamorphic facies according to Bucher and Grapes (2011).

monazite in LR10E sample (central portion),  $615 \pm 6$  Ma for monazite included in peak metamorphic minerals in LR10E sample, and  $632 \pm 4$  Ma for matrix and included monazite in LR44C sample (southern portion).

The textural monazite setting in LR44C sample has no influence on the results and the age (average of  $632 \pm 4$  Ma) is older than those obtained for LR10E sample. The results indicate, therefore, that a single monazite growth episode is registered in rocks from the southern portion. There are two possibilities to explain the older age. It may represent the age of the metamorphic peak associated with the collision of the southern Brasília belt. According to Campos Neto *et al.* (2004, 2010, 2011), rocks from the Carrancas Nappe System are the youngest among all related nappes from the southern Brasília belt, in a continuous migration of the orogen model. Rocks from the Carrancas Nappe System can be lithologically and stratigraphically correlated with the Luminárias Nappe rocks. The age ( $632 \pm 4$  Ma) determined in this paper for LR44C sample is, however, older when compared with those from Carrancas Nappe System (590–575 Ma, U-Pb monazite ages, Valeriano *et al.* 2004, Campos Neto *et al.* 2011). Alternatively, the monazite crystals in LR44C sample may be interpreted as detrital, deriving from metamorphic units within the southern Brasília belt, for example, Socorro-Guaxupé Nappes (Rocha *et al.* 2017), Passos Nappe (Valeriano *et al.* 2004), Carmo da Cachoeira Nappe and Três Pontas-Varginha Nappe (Reno *et al.* 2010, 2012). Reno *et al.* (2012) have presented a comprehensive set of monazite ages for the southern Brasília belt. Oldest ages (662–665 Ma) were obtained for high-pressure granulite from Três Pontas-Varginha Nappe and were interpreted to represent near-peak conditions. Ages of 640–631 Ma are obtained for high yttrium monazite from the same unit and are interpreted as monazite growth from local garnet breakdown. These ages are like those obtained for LR44C sample ( $632 \pm 4$  Ma). In addition, monazite crystals from LR44C sample have the highest yttrium content among all analyzed grains (Fig. 10). Younger ages (616–613 Ma) are presented by Reno *et al.* (2012) for the Carmo da Cachoeira Nappe and the Carvalhos Klippe. For these units, ages younger than 605 Ma are also obtained and are interpreted to be related to the orogenic loading associated with terrane accretion in the Ribeira Belt.

The age difference between included and matrix monazite in LR10E sample is quite significant (*ca.* 15 Ma) and may indicate changes in the tectonometamorphic conditions along the *P-T-t* path. Records of prograde metamorphism steps in garnet porphyroblasts are confirmed by their chemical zoning, as documented by Fumes *et al.* (2017). The older age presented by the included monazite represents the time of garnet and staurolite porphyroblasts crystallization at metamorphic peak conditions. Younger ages are interpreted to represent post-peak monazite crystallization in the rock matrix. A possible interpretation is that monazite grew during a single metamorphic event, during the retrograde part of the *P-T-t* path. An alternative interpretation is that the area faced two metamorphic events, an older one at *ca.* 632–615 Ma, related to the collision of the southern Brasília belt, and a younger one at about 600 Ma related to collision of the Ribeira belt, as proposed in

literature (Trouw *et al.* 2013b, Coelho *et al.* 2017, Reno *et al.* 2012, Peternel *et al.* 2005, Vinagre *et al.* 2016).

Replacement of allanite by monazite is observed in LR10A sample (Fig. 3). LR10A sample is related to the central portion of Luminárias Nappe; it is similar to LR10C sample, a staurolite-biotite-garnet schist. The metamorphic peak assemblage is St + Bt + Grt + Rt and corresponds to high pressure amphibolite facies. According to Gowami-Banerjee & Robyr (2015), the monazite-forming reaction occurs at temperatures higher than  $\sim 600^\circ\text{C}$ , in Barrovian terranes. Although the pressure conditions in Luminárias Nappe rocks are higher than Barrovian terranes, the temperature of  $600^\circ\text{C}$  is near to the peak temperature observed *P-T-t* path of rocks in the northern portion from Luminárias Nappe. According to the calculated pseudosection (Fig. 4A), an invariant curve occurs at *ca.*  $600^\circ\text{C}$ , in which chlorite becomes unstable and biotite is crystallized. The allanite also probably became unstable and the monazite was crystallized close to this reaction.

### Tectonic implications of *P-T-t* path and ages

Pressure conditions of peak metamorphism registered in the Luminárias Nappe rocks indicate that equilibrium took place under conditions that are higher than those of typical Barrovian metamorphism. Therefore, it points to a thick-skinned tectonic setting that is coherent with the continental collision, which may involve subduction of continental crust, proposed for the southern Brasília belt (Dardenne 2000, Fuck *et al.* 2017, Heilbron *et al.* 2017, Tedeschi *et al.* 2017). The ages presented here (Fig. 9) for the Luminárias Nappe rocks ( $615 \pm 6$  Ma — included crystals,  $600 \pm 8$  Ma — matrix crystals for LR10E sample and  $632 \pm 4$  Ma — matrix and included crystals for LR44C sample), are within the time interval of the events that led to the formation of both the southern Brasília belt (630–607 Ma is the age of metamorphic peak according to Rocha *et al.* 2017, Mora *et al.* 2014, Coelho *et al.* 2017, Tedeschi *et al.* 2017, 2018) and the Ribeira belt (620–520 Ma according to Machado *et al.* 1996, Bento dos Santos *et al.* 2007, Heilbron *et al.* 2017). The oldest ages obtained in the present paper are, therefore, in agreement with processes associated with the Brasília orogeny, while younger ages may be related to retrometamorphism or to processes associated with the Ribeira orogeny, extending the interference zone to the study area.

Based on the orogen migration model proposed by Campos Neto *et al.* (2004, 2010, 2011) for the southern Brasília belt, the Carrancas nappe system, which encompasses the studied rocks, corresponds to the last stage of the collision pile and has metamorphic monazite ages of *ca.* 590–575 Ma. The ones presented in this paper, especially those from the southern portion and from the included monazite crystals in the central portion, are considerably older than the ages presented by the authors and, therefore, are inconsistent with the model proposed by Campos Neto *et al.* (2011). However, a word of caution with respect to monazite ages seems appropriate, considering that many reports on such ages show a wide range of results casting some doubt as to the precise meaning of an average monazite age (*e.g.*, Reno *et al.* 2012, Campos Neto *et al.* 2011 and this paper).

In addition, recently published data (Tedeschi *et al.* 2017) on high pressure amphibolite facies mafic rocks from Pouso Alegre (SW of the Luminárias Nappe) indicate that these rocks were metamorphosed at peak *P-T* conditions of  $690 \pm 35^\circ\text{C}$  and  $1.35 \pm 0.30$  GPa. The authors interpret that these rocks represent the deep root of the Ediacaran (630 Ma, U-Pb in zircon and monazite) continent-continent collision zone associated with the Brasília belt. The age and the metamorphic conditions presented here for the southern portion of the Luminárias Nappe agree with the data presented by Tedeschi *et al.* (2017) and may reflect the continental collision associated with the Brasília Belt.

Based on metamorphic and geochronologic data of metamorphic and magmatic rocks from Andrelândia Nappe System (SE of the Luminárias Nappe), Coelho *et al.* (2017) described an orogen-scale interference model for the area, with continental subduction at  $625 \pm 6$  Ma and nappe emplacement at  $618 \pm 5$  Ma, which are both associated with the Southern Brasília Orogen and a second heat pulse associated with Central Ribeira Orogen at  $586 \pm 9$  Ma. Although more detailed geochronological studies need to be carried out, the ages obtained for the southern portion of the Luminárias Nappe ( $632 \pm 4$  Ma), for the included monazite crystals ( $615 \pm 6$  Ma) and for the matrix monazite crystals from the central portion ( $600 \pm 8$  Ma), agree, respectively, with the steps of subduction, nappe emplacement, and heat pulse associated with the Central Ribeira Orogen proposed by Coelho *et al.* (2017).

Sillimanite replacement over kyanite is described in rocks from the southern portion of Luminárias Nappe (Ribeiro & Heilbron 1982, Trouw *et al.* 2000, Peternel *et al.* 2005, Reno *et al.* 2012, Trouw *et al.* 2013b) and is interpreted as a post-peak superposition of deformation and metamorphism associated with the Ribeira belt. Caputo Neto *et al.* (2018) have recently presented data on metasedimentary rocks formed between the late collisional stage of the southern Brasília belt and the main collision in the central Ribeira belt (max. deposition at ca. 611 Ma, evolution range between 611 and 580 Ma). The data presented by the authors suggest that an important uplift through erosion took place in this interval. The decompression associated with the uplift, followed by heating associated with the main collision in the central Ribeira Belt may be responsible for the sillimanite replacement over kyanite. The fact that sillimanite does not occur in any of the studied samples may be related to the whole rock composition. As seen in Figure 4, the lower limit of the peak stability fields for rocks from the central (Bt + St + Grt + Rt) and southern portions (Grt + St + Ky) is strongly controlled by *P*. A decompression to conditions of about 1.0 to 0.9 GPa would lead to the ilmenite crystallization, in the St + Bt + Grt + Ilm stability field, in which neither kyanite nor sillimanite would be present. Ilmenite is indeed present in the studied rocks. An even greater decompression would destabilize garnet in the St + Bt + Ilm field but, still, no aluminum silicate would be present. According to our modeling, a further decompression to conditions of approximately 0.7 GPa, at temperatures between 630 and  $680^\circ\text{C}$ , would be required for the sillimanite crystallization in the studied samples.

The regional metamorphic gradient that is described for the Southern Brasília belt rocks, at the interference zone with the Ribeira belt, is oblique to the main geological contacts

(Trouw *et al.* 1980, Ribeiro & Heilbron 1982, Peternel *et al.* 2005, Reno *et al.* 2012, Trouw *et al.* 2000). This observation is corroborated by our results, since *P-T-t* conditions increase from north to south along the Luminárias Nappe rocks.

One possible scenario to explain the high pressure signature of the studied rocks, as well as the oblique position of the metamorphic gradient in respect to the geological contacts, would be a progressive event that starts with the deformation and metamorphism associated with the Brasília belt and evolves to a collisional, or near collisional, stage (older monazite ages). Our data does not show clearly if the overprint of the younger Ribeira belt occurred before the rocks were exhumed to shallower settings or after uplift and erosion of the Brasília Orogen. In any case, the overprint would be responsible for the oblique metamorphic gradient (tilting of the rock pile in respect to the isotherm and isobar), as well as the younger ages (monazite in the matrix).

The overprint of two distinct tectonic events is not undoubtedly confirmed by the data presented here. It is still possible that the evolution of Luminárias Nappe rocks is associated with one single event entirely related to the Brasília belt event.

## CONCLUSIONS

The metamorphic gradient described in literature for the Luminárias Nappe rock is confirmed through the present paper. In the northern portion, the peak metamorphic condition is ca.  $580 \pm 4^\circ\text{C}$  and ca. 0.9 GPa (high pressure lower amphibolite facies); in the central portion, it is ca.  $600 \pm 15^\circ\text{C}$  and  $1.1 \pm 0.3$  GPa (high pressure amphibolite facies); and in the southern portion, it is ca.  $630 \pm 13^\circ\text{C}$  and  $1.4 \pm 0.6$  GPa (eclogite facies).

Petrographic data, combined with metamorphic modeling, thermobarometry calculations and U-Th-Pb<sub>T</sub> monazite dating indicate that the Luminárias Nappe rocks followed a continuous, single step, clockwise *P-T-t* path.

The peak metamorphic age from Luminárias Nappe is  $615 \pm 6$  Ma for the central portion of Luminárias (LR10E sample) and  $632 \pm 4$  Ma for the southern portion (LR44C sample) according to the included monazite. The age of monazite crystallization in the matrix in the central portion is ca. 15 Ma younger, and there is no difference between the included monazite and matrix monazite in the southern portion.

The integrated approach used in this paper, combining pseudosection modeling and single element thermometers (Zr-in-Rt and Ti-in-Qtz), is a useful tool to constrain the metamorphic conditions.

According to the petrological textures, deformation features, metamorphic conditions and ages presented in this paper, the tectonic evolution of Luminárias Nappe rocks is tightly related to the east-verging orogenic processes of the southern Brasília belt. The effect of the superposition of the younger, northwest-verging, Ribeira belt is interpreted to have caused the tilting of the rock pile in respect to the isotherm and isobars, leading to the formation of an oblique metamorphic gradient. Since kyanite is the only stable Al-silicate, the studied rocks were deformed and metamorphosed under high pressure conditions, which is in compliance with the calculated values of  $630^\circ\text{C}$  and 1.4 GPa for the highest-grade rocks.

## ACKNOWLEDGEMENTS

The authors acknowledge support from São Paulo Research Foundation (FAPESP), through grants 2015/07750-0, 2015/05230-0 and 2016/22627-3, and from the National Council — CNPq (PhD scholarship for RAF- 141604/2018-2).

We would like to thank Thomas Zack for the LA-ICP-MS analysis. The authors are grateful to Rudolph Trouw and an anonymous reviewer for their comments, which improved the article quality. We would like to thank Carlos Grohmann for his attentive editorial handling.

## ARTICLE INFORMATION

Manuscript ID: 20180114. Received on: 10/15/2018. Approved on: 03/30/2019.

R. A. F. wrote the first draft of the manuscript, calculated the pseudosections and prepared all figures. G. L. L. improved the writing of all the manuscript, performed the mineral chemistry and trace elements in rutile analyses at EPMA and the LA-ICP-MS analyses in the quartz, this author is the MsC/PhD supervisor of R. A. F. The author R. M. helped in the metamorphic modelling and petrological interpretations and discussions, revised, and improved the manuscript. M. H. provided improvement in the regional geology writing and the implications of our results in the regional context. S. R. F. V. contributed to the petrochronological analyses in the EPMA, calculated the monazite ages, improved the methods writing and discussions on the ages.

Competing interests: The authors declare no competing interests.

## REFERENCES

- Almeida J.H. 1992. *Mapeamento geológico na Folha Luminárias (MG) 1:50.000 com ênfase na análise estrutural dos metassedimentos do Ciclo Depositional Andrelândia*. MS Dissertation, Instituto de Geociências, Universidade Federal do Rio de Janeiro, Rio de Janeiro, 102 p.
- Araújo Filho J.D. 2000. The Pirineus Syntaxis: An example of the intersection of two Brasiliano fold-thrust belts in central Brazil and its implications for the tectonic evolution of western Gondwana. *Revista Brasileira de Geociências*, **30**(1):144-148.
- Bento dos Santos T., Munhá J., Tassinari C., Fonseca P., Dias Neto C. 2007. Thermochronological evidence for long-term elevated geothermal gradients in Ribeira Belt, SE Brazil. *Geochimica et Cosmochimica Acta*, **71**(15):A79. <https://doi.org/10.1016/j.gca.2007.06.012>
- Bucher K. & Grapes R. 2011. *Petrogenesis of Metamorphic Rocks*. Berlin, Heidelberg, Springer, 428 p.
- Campos Neto M.D.C. 2000. Orogenic Systems from Southwestern Gondwana: an Approach to Brasiliano-Pan African Cycle and Orogenic Collage in Southeastern Brazil. In: Cordani U.G., Milani E.J., Thomaz Filho A., Campos D.A. (Eds.). *Tectonic Evolution of South America*. Rio de Janeiro, Companhia de Pesquisa de Recursos Minerais, p. 335-365.
- Campos Neto M.D.C. & Caby R. 1999. Neoproterozoic high-pressure metamorphism and tec-tonic constraint from the nappe system south of the Sao Francisco Craton, southeast Brazil. *Precambrian Research*, **97**(1-2):3-26. [https://doi.org/10.1016/S0301-9268\(99\)00010-8](https://doi.org/10.1016/S0301-9268(99)00010-8)
- Campos Neto M.D.C., Basei M.A.S., Janasi V.D., Moraes R. 2011. Orogen mi-gration and tectonic setting of the Andrelândia Nappe system: An Ediacaran western Gondwana collage, south of São Francisco craton. *Journal of South American Earth Sciences*, **32**(4):393-406. <https://doi.org/10.1016/j.jsames.2011.02.006>
- Campos Neto M.D.C., Basei M.A.S., Vlach S.R.F. Caby R., Szabó G.A.J., Vasconcelos P. 2004. Migração de Orógenos e Superposição de Orogêneses: Um Esboço da Colagem Brasileira no Sul do Cráton do São Francisco, SE - Brasil. *Geologia USP - Série Científica*, **4**(1):13-40. <https://doi.org/10.5327/S1519-874x2004000100002>
- Campos Neto M.D.C., Cioffi C.R., Moraes R., Motta R.G., Siga Jr. O., Basei M.A.S. 2010. Structural and metamorphic control on the exhumation of high-P granulites: The Carvalhos Klippe example, from the oriental Andrelândia Nappe System, southern portion of the Brasília Orogen, Brazil. *Precambrian Research*, **180**(3-4):125-142. <https://doi.org/10.1016/j.precamres.2010.05.010>
- Campos Neto M.D.C., Janasi V.A., Basei M.A.S., Siga Jr. O. 2007. Sistema de nappes Andrelândia, setor oriental: litoestratigrafia e posição estratigráfica. *Revista Brasileira de Geociências*, **37**(4 Suppl.):47-60.
- Caputo Neto V., Ribeiro A., Nepomuceno F.O., Dussin I.A., Trouw R.A.J. 2018. The Pico do Itapeva Formation: A record of gravitational flow deposits in an Ediacaran intracontinental basin, southern Brasília Orogen, SE Brazil. *Journal of South American Earth Sciences*, **84**:34-47. <http://dx.doi.org/10.1016/j.jsames.2018.03.006>
- Cherniak D., Manchester J., Watson E. 2007. Zr and Hf diffusion in rutile. *Earth and Planetary Science Letters*, **261**(1):267-279. <https://doi.org/10.1016/j.epsl.2007.06.027>
- Cherniak D. 2000. Pb diffusion in rutile. *Contributions to Mineralogy and Petrology*, **139**(2):198-207. <https://doi.org/10.1007/PL00007671>.
- Coelho M.B., Trouw R.A.J., Araújo C.E.G., Vinagre R., Mendes J.C., Sato K. 2017. Constraining timing and P-T conditions of continental collision and late overprinting in the Southern Brasília Orogen (SE-Brazil): U-Pb zircon ages and geothermobarometry of the Andrelândia Nappe System. *Precambrian Research*, **292**:194-215. <http://dx.doi.org/10.1016/j.precamres.2017.02.001>
- Cruz-Urbe A.M., Feineman M.D., Zack T., Jacob D.E. 2018. Assessing trace element (dis) equilibrium and the application of single element thermometers in metamorphic rocks. *Lithos*, **314-315**:1-15. <https://doi.org/10.1016/j.lithos.2018.05.007>
- Dardenne M.A. 2000. In: Cordani U.G., Milani E.J., Thomaz-Filho A., Campos D.A. (Eds.). *Tectonic evolution of South America. 31st International Geological Congress*. Rio de Janeiro, p. 231-264.
- Ebert H. 1956. Relatório de atividades. *Relatório Anual do Diretor da Divisão de Geologia e Mineralogia*. Rio de Janeiro: DNPM, p. 62-107.
- Engi M., Lanari P., Kohn M.J. 2017. Significant ages—an introduction to petrochronology. *Reviews in Mineralogy and Geochemistry*, **83**(1):1-12. <https://doi.org/10.2138/rmg.2017.83.1>
- Fraser G., Ellis D., Eggins S. 1997. Zirconium abundance in granulite-facies minerals, with implications for zircon geochronology in high-grade rocks. *Geology*, **25**(7):607-610. [https://doi.org/10.1130/0091-7613\(1997\)025%3C0607:ZAI GFM%3E2.3.CO;2](https://doi.org/10.1130/0091-7613(1997)025%3C0607:ZAI GFM%3E2.3.CO;2)
- Fuck R.A., Pimentel M.M., Alvarenga C.J.S., Dantas E.L. 2017. The northern Brasília belt In: Heilbron M., Cordani U.G., Alkmim F.F. (Eds.). *São Francisco Craton, Eastern Brazil Tectonic Genealogy of a Miniature Continent, Regional Geology Reviews*, Berlin Heidelberg, Springer, p. 205-220.
- Fumes R.A. 2017. *Modelagem metamórfica e geotermobarometria de elementos traço em metapelitos e quartzitos: exemplo da Nappe de Luminárias-MG*. MS Dissertation, Instituto de Geociências e Ciências Exatas, Universidade Estadual de São Paulo, Rio Claro, 140 p.
- Fumes R.A., Luvizotto G.L., Moraes R., Ferraz E.R.M. 2017. Petrografia, Química Mineral e Geotermobarometria dos Metapelitos do Grupo Carrancas na Nappe de Luminárias (MG). *Geociências*, **36**(4):639-654.
- Goswami-Banerjee S. & Robyr M. 2015. Pressure and temperature conditions for crystallization of metamorphic allanite and monazite in metapelites: a case study from the Miyar Valley (high Himalayan Crystalline of Zaskar, NW India). *Journal of Metamorphic Geology*, **33**(5):535-556. <https://doi.org/10.1111/jmg.12133>

- Hart E., Storey C., Harley S.L., Fowler M. 2018. A window into the lower crust: Trace element systematics and the occurrence of inclusions/intergrowths in granulite-facies rutile. *Gondwana Research*, **59**:76-86. <https://doi.org/10.1016/j.gr.2018.02.021>
- Hasui Y., Carneiro C.D.R., Coimbra A.M. 1975. The Ribeira folded belt. *Revista Brasileira de Geociências*, **5**(4):257-266.
- Heilbron M., Mohriak W., Valeriano C.M., Milani E., Almeida J.C., Tupinambá M. 2000. From Collision to extension: the roots of the south-eastern continental margin of Brazil. In: Talwani M., Mohriak W. (Eds.). *Atlantic Rifts and Continental Margins of Brazil*, 115<sup>th</sup> ed., *Geophysical Monographs*, American Geophysical Union, p. 1-34.
- Heilbron M., Pedrosa Soares A.C., Campos Neto M.D.C., Silva L.D., Trouw R.A.J., Janasi V.A., Mantesso Neto V., Bartorelli A., Carneiro C., Brito Neves B.B. 2004. Província Mantiqueira. In: Mantesso-Neto V., Bartorelli A., Carneiro C.D.R., Brito-Neves B.B. (Eds.). *Geologia do Continente sul-americano: evolução da obra de Fernando Flávio Marques de Almeida*. São Paulo, Beca, p. 203-235.
- Heilbron M., Ribeiro A., Valeriano C.M., Paciullo F.V.P., Almeida J.C., Trouw R.A.J., Tupinambá M., Eirado Silva L.G. 2017. The Ribeira belt. In: Heilbron M., Cordani U.G., Alkmim F.F. (Eds.). *São Francisco Craton, Eastern Brazil Tectonic Genealogy of a Miniature Continent*, *Regional Geology Reviews*. Berlin, Heidelberg, Springer, p. 277-302.
- Heilbron M., Valeriano C.M., Tassinari C., Almeida J., Tupinambá M., Siga O., Trouw R.A.J. 2008. Correlation of Neoproterozoic terrane between the Ribeira Belt, SE Brazil and its African counterpart: comparative tectonic evolution and open questions. *Geological Society, London, Special Publications*, **294**:211-237. <https://doi.org/10.1144/SP294.12>
- Holland T.J.B. & Powell R. 2000. AX: A program to calculate activities of mineral end members from chemical analyses (usually determined by electron microprobe). Available at: <<https://www.esc.cam.ac.uk/research/research-groups/research-projects/tim-hollands-software-pages/ax>>. Accessed on: May 8, 2017.
- Holland T.J.B. & Powell R. 2011. An improved and extended internally consistent thermodynamic dataset for phases of petrological interest, involving a new equation of state for solids. *Journal of Metamorphic Geology*, **29**(3):333-383. <https://doi.org/10.1111/j.1525-1314.2010.00923.x>
- Kohn M.J., Penniston-Dorland S.C., Ferreira J.C. 2016. Implications of near-rim compositional zoning in rutile for geothermometry, geospeedometry, and trace element equilibration. *Contributions to Mineralogy and Petrology*, **171**(10):78. <http://dx.doi.org/10.1007/s00410-016-1285-1>
- Kooijman E., Mezger K., Berndt J. 2010. Constraints on the U–Pb systematics of metamorphic rutile from in situ LA-ICP-MS analysis. *Earth and Planetary Science Letters*, **293**(3-4):321–330. <https://doi.org/10.1016/j.epsl.2010.02.047>
- Kretz R. 1983. Symbols for rock-forming minerals. *American Mineralogist*, **68**:277-279.
- Luvizotto G.L. & Zack T. 2009. Nb and Zr behavior in rutile during high-grade metamorphism and retrogression: an example from the Ivrea–Verbano Zone. *Chemical Geology*, **261**(3-4):303-317. <https://doi.org/10.1007/s00710-009-0092-z>
- Luvizotto G.L., Zack T., Triebold S., Von Eynatten H. 2009. Rutile occurrence and trace element behavior in medium-grade metasedimentary rocks: Example from the Erzgebirge, Germany. *Mineralogy and Petrology*, **97**(3-4):233-249. <https://doi.org/10.1007/s00710-009-0092-z>
- Machado N., Valladares C., Heilbron M., Valeriano C. 1996. U Pb geochronology of the central Ribeira belt (Brazil) and implications for the evolution of the Brazilian Orogeny. *Precambrian Research*, **79**(3-4):347-361. [https://doi.org/10.1016/0301-9268\(95\)00103-4](https://doi.org/10.1016/0301-9268(95)00103-4)
- Möller C., Majka J., Janák M., Van Roermund H. 2018. High-and ultrahigh-pressure rocks-keys to lithosphere dynamics. *Journal of Metamorphic Geology*, **36**(5):511-515. <https://doi.org/10.1111/jmg.12421>
- Mora C.A.S., Neto M.D.C.C., Basei M.A.S. 2014. Syn-collisional lower continental crust anatexis in the Neoproterozoic Socorro-Guaxupé Nappe System, southern Brasília Orogen, Brazil: Constraints from zircon U–Pb dating, Sr–Nd–Hf signatures and whole-rock geochemistry. *Precambrian Research*, **255**: 847-864. <https://doi.org/10.1016/j.precamres.2014.10.017>
- Moraes R., Brown M., Fuck R.A., Camargo M.A., Lima T.M. 2002. Characterization and P-T Evolution of Melt-bearing Ultrahigh-temperature Granulites: an Example from the Anapolis-Itaçu Complex of the Brasília Fold Belt, Brazil. *Journal of Petrology*, **43**(9):1673-1705. <https://doi.org/10.1093/petrology/43.9.1673>
- Moraes R., Niccolett C., Barbosa J.S.F., Fuck R.A., Sampaio A.R. 2015. Applications and limitations of thermobarometry in migmatites and granulites using as an example rocks of the Araçaí Orogen in southern Bahia, including a discussion on the tectonic meaning of the current results. *Brazilian Journal of Geology*, **45**(4):517-539. <http://dx.doi.org/10.1590/2317-4889201520150026>
- Nunes R.P.M., Trouw R.A.J., Castro E.O. 2008. *Mapa Geológico - Folha Varginha – escala 1:100.000*, Programa Geologia do Brasil. Brasil, Serviço Geológico do Brasil.
- Paciullo F.V.P. & Ribeiro A. 2008. *Mapa Geológico-Folha Nepumoceno*. Escala 1:100.000. Rio de Janeiro, Universidade Federal do Rio de Janeiro/Serviço Geológico do Brasil.
- Paciullo F.V.P., Ribeiro A., Andreis R.R., Trouw R.A.J. 2000. The Andrelândia Basin, a Neoproterozoic Intraplate Continental Margin, Southern Brasília Belt, Brazil. *Revista Brasileira de Geociências*, **30**(1):200-202.
- Paciullo F.V.P., Ribeiro A., Trouw R.A.J. 2003. *Geologia da Folha Andrelândia, escala 1:100.000*. Texto explicativo. Geologia e recursos minerais do sudeste mineiro. Projeto Sul de Minas - Etapa I. Brasil, Serviço Geológico do Brasil, 84-119 p.
- Passchier C.W. & Trouw R.A.J. 2005. *Microtectonics*. Heidelberg, Springer, 366 p.
- Peternel R., Trouw R.A.J., Schmitt R.D.S. 2005. Interferência entre duas faixas móveis neoproterozóicas: o caso das faixas Brasília e Ribeira no sudeste do Brasil. *Brazilian Journal of Geology*, **35**(3):297-310.
- Powell R. & Holland T.J.B. 1988. An internally consistent dataset with uncertainties and correlations: 3. Applications to geobarometry, worked examples and a computer program. *Journal of Metamorphic Geology*, **6**(2):173-204. <https://doi.org/10.1111/j.1525-1314.1988.tb00415.x>
- Powell R., Holland T., Worley B. 1998. Calculating phase diagrams involving solid solutions via non-linear equations, with examples using THERMOCALC. *Journal of Metamorphic Geology*, **16**(4):577-588. <https://doi.org/10.1111/j.1525-1314.1998.00157.x>
- Quémener J.J.G., Ribeiro A., Paciullo F.V.P., Heilbron M., Trouw R.A.J., Valença J.G., Noce C.M. 2002. *Projeto Sul de Minas - etapa 1: Mapa Geológico-Folha Lavras, escala 1:100.000*. Minas Gerais, CODEMIG.
- Reno B.L., Brown M., Piccoli P.M. 2010. <sup>40</sup>Ar/<sup>39</sup>Ar thermochronology of high-pressure granulite nappes in the southern Brasília belt, Brazil: Implications for nappe exhumation. *American Journal of Science*, **310**(10):1294-1332. <https://doi.org/10.2475/10.2010.04>
- Reno B.L., Piccoli P.M., Brown M., Trouw R.A.J. 2012. In situ monazite (U-Th)-Pb ages from the Southern Brasília Belt, Brazil: Constraints on the high-temperature retro-grade evolution of HP granulites. *Journal of Metamorphic Geology*, **30**(1):81-112. <https://doi.org/10.1111/j.1525-1314.2011.00957.x>
- Ribeiro A. & Heilbron M. 1982. Estratigrafia e Metamorfismo dos Grupos Carrancas e Adrelândia, Sul de Minas Gerais. In: Congresso Brasileiro de Geologia, 32. *Actas...* v. 1. P. 177-186.
- Ribeiro A., Trouw R.A.J., Andreis R.R., Paciullo F.V.P., Valença J.G. 1995. Evolução das Bacias Proterozóicas e o Termo-Tectonismo Brasileiro na Margem Sul do Cráton do São Francisco. *Revista Brasileira de Geociências*, **25**(4):235-248.
- Rocha B.C., Moraes R., Möller A., Cioffi C.R. 2018. Magmatic inheritance vs. UHT metamorphism: Zircon petrochronology of granulites and petrogenesis of charnockitic leucosomes of the Socorro–Guaxupé nappe, SE Brazil. *Lithos*, **314**:16-39. <https://doi.org/10.1016/j.lithos.2018.05.014>
- Rocha B., Moraes R., Möller A., Cioffi C., Jercinovic M. 2017. Timing of anatexis and melt crystallization in the Socorro–Guaxupé nappe, SE Brazil: Insights from trace element composition of zircon, monazite and garnet coupled to U-Pb geochronology. *Lithos*, **277**:337-355. <https://doi.org/10.1016/j.lithos.2016.05.020>
- Silva M.P. 2010. *Modelamento Metamórfico de Rocas das Fácies Xisto-Verde e Anfibolito com o Uso de Pseudosseções: Exemplo das Rochas da Klippe Carrancas, Sul de Minas Gerais*. MS Dissertation, Instituto de Geociências, Universidade de São Paulo, São Paulo, 144 p.

- Spencer C.J., Hawkesworth C., Cawood P.A., Dhuime B. 2013. Not all supercontinents are created equal: Gondwana-rodinia case study. *Geology*, **41**(7):795-798. <https://doi.org/10.1130/G34520.1>
- Stendal H., Toteu S.F., Frei R., Penaye J., Njel U.O., Bassahak J., Nni J., Kankeu B., Ngako V., Hell J.V. 2006. Derivation of detrital rutile in the Yaounde region from the Neoproterozoic Pan-African belt in southern Cameroon (central Africa). *Journal of African Earth Sciences*, **44**(4):443-458. <http://dx.doi.org/10.1016/j.jafrearsci.2005.11.012>
- Tedeschi M., Lanari P., Rubatto D., Pedrosa-Soares A., Hermann J., Dussin I., Pinheiro M.A.P., Bouvier A.S., Baumgartner L. 2017. Reconstruction of multiple P-T-t stages from retrogressed mafic rocks: Subduction versus collision in the southern Brasília orogen (SE Brazil). *Lithos*, **294**:283-303. <https://doi.org/10.1016/j.lithos.2017.09.025>
- Tedeschi M., Pedrosa-Soares A., Dussin I., Lanari P., Novo T., Pinheiro M.A.P., Lana C., Peters D. 2018. Protracted zircon geochronological record of UHT garnet-free granulites in the southern Brasília orogen (SE Brazil): petrochronological constraints on magmatism and metamorphism. *Precambrian Research*, **316**:103-126. <https://doi.org/10.1016/j.precamres.2018.07.023>
- Thomas J.B., Watson E.B., Spear F.S., Shemella P.T., Nayak S.K., Lanzirotti A. 2010. Titanium under pressure: The effect of pressure and temperature on the solubility of Ti in quartz. *Contribution to Mineralogy and Petrology*, **160**(5):743-759. <http://dx.doi.org/10.1007/s00410-010-0505-3>
- Tomkins H.S., Powell R., Ellis D.J. 2007. The pressure dependence of the zirconium-in-rutile thermometer. *Journal of Metamorphic Geology*, **25**(6):703-713. <https://doi.org/10.1111/j.1525-1314.2007.00724.x>
- Triebold S., Von Eynatten H., Luvizotto G. L., Zack T. 2007. Deducing source rock lithology from detrital rutile geochemistry: An example from the Erzgebirge, Germany. *Chemical Geology*, **244**(3-4):421-436. <http://dx.doi.org/10.1016/j.chemgeo.2007.06.033>
- Triebold S., Von Eynatten H., Zack T. 2012. A recipe for the use rutile in sedimentary provenance analysis. *Sedimentary Geology*, **282**:268-275. <http://dx.doi.org/10.1016/j.sedgeo.2012.09.008>
- Trouw R.A.J., Heilbron M., Ribeiro A., Paciullo F.V.P., Valeriano C.M., Almeida J.C.H., Tupinambá M., Andreis R.R. 2000. The Central Segment of the Ribeira Belt. In: Cordani U.G., Milani E.J., Thomaz Filho A., Campos D.A. (Eds.). *Tectonic Evolution of South America*. Brasil, Companhia de Pesquisa de Recursos Minerais, p. 287-310.
- Trouw R.A.J., Paciullo F.V.P., Ribeiro A., Bittar S., Almeida J.C.H. 2013a. *Mapa Geológico-Folha Caxambu*. Projeto Sul de Minas - etapa 1, escala 1:100.000. Belo Horizonte, CODEMIG.
- Trouw R.A.J., Peternel R., Ribeiro A., Heilbron M., Vinagre R., Duffles P., Trouw C.C., Fontainha M., Kussama H.H. 2013b. A new interpretation for the interference zone between the southern Brasília belt and the central Ribeira belt, SE Brazil. *Journal of South American Earth Sciences*, **48**:43-57. <https://doi.org/10.1016/j.jsames.2013.07.012>
- Trouw R.A.J., Ribeiro A., Paciullo F.V.P. 1980. Evolução Estrutural e Metamórfica de uma área a SE de Lavras - Minas Gerais. In: Congresso Brasileiro de Geologia. Balneário de Camboriú, 31., Santa Catarina. *Actas...* v. 30. p. 2773-2784.
- Trouw R.A.J., Ribeiro A., Paciullo F.V.P. 1983. Geologia Estrutural do Grupos São João del Rei, Carrancas e Andrelândia, Sul de Minas Gerais. *Anais da Academia Brasileira de Ciências*, **55**(1):71-87.
- Trouw R.A.J., Tavares F.M., Robyr M. 2008. Rotated garnets: a mechanism to explain the high frequency of inclusion trail curvature angles around 90° and 180°. *Journal of Structural Geology*, **30**(8):1024-1033. <http://dx.doi.org/10.1016/j.jsg.2008.04.011>
- Valeriano C., Machado N., Simonetti A., Vallares C.S., Seer H.J., Simões L.S. 2004. U-Pb Geochronology of Southern Brasília Belt (SE Brazil): sedimentary provenance, Neoproterozoic orogeny and assembly of Western Gondwana. *Precambrian Research*, **130**(1-4):27-55. <http://dx.doi.org/10.1016/j.precamres.2003.10.014>
- Valeriano C.M. 2017. The southern Brasília belt. In: Heilbron M., Cordani U.G., Alkmim F.F. (Eds.). São Francisco Craton, Eastern Brazil Tectonic Genealogy of a Miniature Continent. *Regional Geology Reviews*, Berlin, Heidelberg, Springer, p. 189-203.
- Vinagre R., Trouw R.A.J., Kussama H., Peternel R., Mendes J.C., Duffles P. 2016. Superposition of structures in the interference zone between the southern Brasília belt and the central Ribeira belt in the region SW of Itajubá (MG), SE Brazil. *Brazilian Journal of Geology*, **46**(4):547-566. <http://dx.doi.org/10.1590/2317-4889201620160034>
- Vlach S.R.F. 2010. Th-U-Pb<sub>T</sub> dating by electron probe microanalysis, part I. Monazite: analytical procedures and data treatment. *Geologia USP: Série Científica*, **10**(1):61-85. <https://doi.org/10.5327/z1519-874x2010000100006>
- Vlach S.R.F. & Gualda G.A.R. 2000. Microprobe monazite dating and the ages of some granitic and metamorphic rocks from southeastern Brazil. *Revista Brasileira de Geociências*, **30**(1):214-218.
- Westin A., Campos Neto M.C. 2013. Provenance and tectonic setting of the external nappe of the Southern Brasília Orogen. *Journal of South American Earth Sciences*, **48**:220-239. <http://dx.doi.org/10.1016/j.jsames.2013.08.006>
- Westin A., Campos Neto M.C., Cawood P.A., Hawkesworth C.J., Dhuime B., Delavault H. 2019. The Neoproterozoic southern passive margin of the São Francisco craton: Insights on the pre-amalgamation of West Gondwana from U-Pb and Hf-Nd isotopes. *Precambrian Research*, **320**:454-471. <https://doi.org/10.1016/j.precamres.2018.11.018>
- Westin A., Campos Neto M.C., Hawkesworth C.J., Cawood P.A., Dhuime B., Delavault H. 2016. A paleoproterozoic intra-arc basin associated with a juvenile source in the southern Brasília orogen: Application of U-Pb and Hf-Nd isotopic analyses to provenance studies of complex areas. *Precambrian Research*, **276**:178-193. <https://doi.org/10.1016/j.precamres.2016.02.004>
- White R.W., Powell R., Holland T.J.B., Johnson T.E., Green E.C.R. 2014. New mineral activity-composition relations for thermodynamic calculations in metapelitic systems. *Journal of Metamorphic Geology*, **32**(3):261-286. <https://doi.org/10.1111/jmg.12071>
- White R.W., Powell R., Holland T.J.B., Workley B.A. 2000. The effect of TiO<sub>2</sub> and Fe<sub>2</sub>O<sub>3</sub> on metapelitic assemblages at greenschist and amphibolite facies conditions: mineral equilibria calculations in the system K<sub>2</sub>O-FeO-MgO-Al<sub>2</sub>O<sub>3</sub>-SiO<sub>2</sub>-H<sub>2</sub>O-TiO<sub>2</sub>-Fe<sub>2</sub>O<sub>3</sub>. *Journal of Metamorphic Geology*, **18**(5):497-512. <http://dx.doi.org/10.1046/j.1525-1314.2000.00269.x>
- Williams M., Jercinovic M., Gonçalves P., Mahan K. 2006. Format and philosophy for collecting, compiling, and reporting microprobe monazite ages. *Chemical Geology*, **225**(1-2):1-15. <http://dx.doi.org/10.1016/j.chemgeo.2005.07.024>
- Zack T., Moraes R., Kronz A. 2004. Temperature dependence of Zr in rutile: Empirical calibration of a rutile thermometer. *Contributions to Mineralogy and Petrology*, **148**(4):471-488. <http://dx.doi.org/10.1007/s00410-004-0617-8>